S.T. Chong, M. Hassanaly, H. Koo, M.E. Mueller, V. Raman, K.P. Geigle, Large eddy simulation of pressure and dilution-jet effects on soot formation in a model aircraft swirl combustor, Combust. Flame 192 (2018) 452-472

http://dx.doi.org/j.combustflame.2018.02.021

Large Eddy Simulation of Pressure and Dilution-jet Effects on Soot Formation in a Model Aircraft Swirl Combustor

Shao Teng Chong[a], Malik Hassanaly[a], Heeseok Koo[a], Michael E. Mueller[b], Venkat Raman[a], Klaus-Peter Geigle[c]

[a]*Department of Aerospace Engineering, University of Michigan, Ann Arbor, MI 48109, USA*
[b]*Department of Mechanical and Aerospace Engineering, Princeton University, Princeton, NJ 08544, USA*
[c]*German Aerospace Center (DLR) Institution of Combustion Technology, Pfaffenwaldring 38-40, D-70569, Stuttgart, Germany*

Abstract

Soot formation in a model aircraft engine configuration operating at elevated pressures is studied using large eddy simulation (LES) and detailed models for precursor and soot population evolution. Specifically, pressure and secondary oxidation air injection effects on soot formation are simulated. The configuration simulated is a dual-swirl ethylene/air combustor operating at pressures of 3 and 5 bars, with and without secondary oxidation air injection. The inflow conditions are chosen such that for the two different pressures, the only hydrodynamic change is the Reynolds number. Detailed comparisons with experimental data show that the simulation captures gas-phase statistics accurately. Although the spatial structure of soot formation is captured, including some of the trends for different operating conditions, the quantitative comparisons had significant differences. This could be attributed to the large distribution in the measurements or the chemical/physical models for soot formation. Detailed analysis showed that soot mass generation in such devices is driven by acetylene-based surface growth, with strong oxidation zones that significantly reduce net soot emissions. More importantly, soot formation occurs due to a spatially and temporally intermittent phenomena, where a small set of fluid trajectories that deposit fuel-rich pockets into the right gas-phase conditions is responsible for the bulk of soot mass generated. The occurrence of these relatively low-frequency trajectories is due to large scale unsteadiness caused by the strong swirl near the fuel jets. Lagrangian particle trajectory analysis revealed that lower pressure case without sidejet injection encourages entrainment of soot particles into the inner recirculation zone, increasing the residence time and leading to increased soot volume fraction. When pressure is increased from 3 to 5 bar, these particles move through a different mixture fraction-progress variable phase space. Consequently, there is a hydrodynamic scaling mode introduced, which can produce interesting variations from the nominal pressure scaling for soot production. These studies point to an intricate dependence of soot formation on large-scale turbulent flows, which is generally non-universal and not observed in canonical jet flames.

Keywords: Large eddy simulation, detailed soot model, high pressure combustor, hybrid method of moments, swirl combustor

1. Introduction

With increase in operating pressures of aircraft combustors, it is expected that there will be an accompanying increase in particulate emissions [1]. Although modern combustors operate at globally lean equivalence ratios, locally inefficient turbulent mixing can lead to fuel-rich pockets that promote particulate formation. Understanding the role of such mixing processes and the effect of pressure increase on soot emissions is critical for the development of next generation gas turbines. In this context, detailed computational modeling is a useful tool. However, developing predictive computational models for soot is recognized as a formidable challenge [2, 3]. Due to the high Reynolds number turbulent flow within an aircraft combustor, soot formation is intricately linked to the turbulence-chemistry interaction associated with both fuel oxidation and soot evolution processes. Although significant progress has been made in the modeling of soot formation in flames [4, 5], application of these tools to realistic gas turbine flows and direct comparison with experiments remains sparse. The focus of this work is to use state-of-the-art tools for modeling turbulence, combustion, and soot evolution processes to simulate a model aircraft combustor, operating at elevated pressures. The objective is to determine the predictive capability of the models and analyze the challenges in capturing soot formation in complex flows.

It is now accepted that the use of large eddy simulation (LES) is necessary to capture the turbulent mixing driven combustion processes that govern aircraft-type combustors [6]. In particular, LES has been applied to model gas-phase combustion in a variety of aircraft combustor geometries, with very good success in the prediction of the overall flow characteristics [7–11]. In many of these applications, the use of tabulated flamelet approaches has been shown to be accurate for operating conditions far away from blowout or other extinction phenomena [8, 12–14]. For this reason, in this work, LES with flamelet approach is used to model the turbulent combustion process. The simulation of soot formation is itself a complex problem. This includes the chemical and physical models that govern gas-phase precursor and particulate-phase evolution [3, 15, 16], as well as the computational description of the nanoparticle population balance [5, 17–19]. Aided by increasing computational power, detailed models as well as the framework for such comprehensive simulations have been developed [3, 20–22]. Here, the soot modeling approach of Mueller et al. [3] will be utilized. This method incorporates detailed chemical kinetics for the fuel oxidation and precursor formation, turbulence-chemistry interaction using a presumed-PDF approach [23], and nanoparticle evolution through the method-of-moments [19, 24].

Over the last decade, validation studies that utilize high-fidelity experimental data have emerged for sooting flames. The International Sooting Flames Workshop (ISF) [25] provides one such central forum for model validation. An analysis of results presented there and elsewhere [20–22, 26, 27] provides interesting insights. Canonical jet flames, which are amongst the simplest turbulent flows that support chemical reactions, are found to be a challenging configuration for soot prediction. While there are numerous literature studies demonstrating the accuracy of LES in predicting gas-phase jet flames [6, 28, 29], similar computational models fail to predict soot concentrations spectacularly, often providing volume fractions that are orders of magnitude lower (or higher) compared to experiments [25]. Part of this discrepancy is due to the high sensitivity of soot formation to gas-phase thermochemical composition. For instance, Mueller and Raman [30] have shown that even small errors in temperature mismatch with experiments can lead to significant errors in soot predictions. Further, models for soot evolution are often formulated based on data from laminar flames, which may not be representative of the conditions seen in a turbulent flame. This includes the range of strain rates, as well as the spatial and temporal variations in the thermochemical composition of the gas-phase, which introduces a history-dependent evolution of the soot particles.

Since different physical and chemical processes dictate soot formation, the relative importance as well as accuracy determine predictive capability. Temperature perturbations resulted in downstream soot volume fraction errors of 30% in turbulent nonpremixed piloted jet flames [30], however this was insufficient to explain the discrepancies with experimental data. Other sources of error in turbulent combustion modeling or chemistry mechanism are likely responsible as well. In jet flames burning ethylene fuel, models that employ Polycyclic Aromatic Hydrocarbon (PAH) based precursor chemistry vastly underpredict soot volume fraction [25]. On the other hand, semi-empirical models [31] that rely on acetylene-based nucleation predict much higher soot mass [20]. Since PAH concentrations are highly sensitive to strain rates, it is possible that either inaccurate precursor chemistry or errors in models for small-scale dissipation/strain rates leads to this discrepancy. On the contrary, bluff-body stabilized flames are well represented even by PAH-based models, where surface growth by an acetylene-addition mechanism dominates [15, 16, 26]. Consequently, there is some uncertainty in the cause of model discrepancy.

Since aircraft engines form one class of end application for these models, it is imperative to test predictive capability in near-realistic conditions. The DLR model aircraft combustor experiments [32] provide high-fidelity measurements such as three-component flow field, temperature, and soot volume fraction statistics, ideal for testing detailed computational models. In particular, the combustor allows secondary air injection, which emulates dilution jets in rich-quench-lean type aircraft combustors. This combustor configuration has been previously simulated using unsteady Reynolds-Averaged Navier Stokes (URANS) approach [33, 34] and LES techniques [13, 35]. The URANS study used a semi-empirical soot model, combined with finite chemistry, sectional description of PAH, along with conventional turbulence models, and was able to capture the location of soot formation. The LES calculations showed similar fidelity, capturing the gas-phase flow field and soot locations quite accurately. Still, the LES approach overpredicted soot volume fraction by a factor ranging from 2 to an order of magnitude.

The focus of the current study is to simulate the DLR configuration at higher operating pressures of 3 and 5 bar. For each of these conditions, simulations with and without sidejet injection were considered. The focus is on understanding the relative importance of different physical and chemical processes that lead to soot generation, evolution, and destruction. The rest of the sections are laid out as follows. First, in Sec. 2, the experimental configuration and operating conditions are discussed. Next, in Sec. 3, the models and computational tools are described, followed by details of the numerical approach. The results of the simulations and an analysis of the comparison with experiments are provided in Sec. 4. Specifically, effects of sidejet and pressure are analyzed and comparisons of current soot scaling with canonical laminar flames [36] is performed. Finally, a summary of findings is presented in Sec. 5. Details of the fully unstructured mesh with refinement at the inlet and the grid convergence are shown in Appendix A. Temporal convergence of flow and soot statistics are presented in Appendix B.

2. Experimental Configuration

The ethylene-based DLR model aircraft combustor configuration is shown schematically in Fig. 1, adapted from Geigle et al. [37]. The main combustion chamber measures 120 mm in height and has a square section of 68×68 mm^2. The inlet oxidizer air is introduced in two streams, through a central nozzle with a diameter of 12.3 mm and a ring injector with inner and outer diameters of 14.4 mm and 19.8 mm. The inflow consists of an intricate set of swirlers to inject the oxidizer jets with tangential velocities. The fuel ports consist of 60 straight channels (fuel port area = 0.5×0.4 mm^2) which are located between these two oxidizer streams. A set of injector ports are located on the posts at the height of 80 mm that radially introduce secondary air similar to the rich-quench-lean design for aircraft combustors.

The four different cases discussed in this work correspond to flow conditions provided in Table 1. Comparisons of 3 and 5 bar pressures with equivalent inlet fuel and oxidizer velocities are studied in this work. Moreover, comparisons with and without secondary oxidation air are also discussed. The ratio of mass flow rate between the central and ring air inlets was fixed at 3/7. However, the velocities of all the streams are constant for the different pressure cases, which implies that the jet-exit strain rates do not change, but the Reynolds number increases with pressure. This retains the integral time scale that controls residence time in the reactor but reduces the small-scale mixing time scale. Further details about the experimental configuration and measurement techniques are provided in [32, 37, 38]. The soot laser-induced incandescence (LII) measurement uncertainty is declared to be 30 %, temperature coherent anti-Stokes Raman scattering (CARS) measurement uncertainty is 5 %, and velocity particle image velocimetry (PIV) measurement uncertainty for the conditions studied are difficult to evaluate because they are strongly dependent on the location in the combustor and (instantaneous) interferences of other effects.

3. Model Details

The DLR swirl combustor is simulated using the LES approach. The gas-phase combustion is described using a radiation flamelet/progress variable (RFPV) approach, where a set of unsteady one-dimensional flamelets are tabulated for look-up in the computation [3, 23]. In addition to the steady flamelet solutions, the unsteady flamelet solutions are included for parameterizing with respect to a heat loss parameter H to account for enthalpy loss through radiation effects [39]. In addition, an explicit transport equation is solved for the combined mass fraction of PAH. For further details of the conservation equations, the reader is referred to previous articles [23, 39, 40]. The transport equation for additional conserved scalars and thermochemical properties, namely, mixture fraction Z, progress variable C, and the heat loss parameter H are described in Eq 1.

$$\frac{\partial \rho \kappa}{\partial t} + \frac{\partial \rho u_j \kappa}{\partial x_j} = \frac{\partial}{\partial x_j}\big(\rho D \frac{\partial \kappa}{\partial x_j}\big) + \rho S(\kappa), \tag{1}$$

where $\kappa = \{Z, C, H, Y_{PAH}\}$. These equations are filtered to derive their LES counterparts, and this leads to unclosed terms, models for which are described in Mueller and Pitsch [39]. The flamelet equations are solved and the solutions stored in a flamelet table for lookup of the source terms, $S(\kappa) = \{S_Z, S_C, S_H, S_{Y_{PAH}}\}$. The gas-phase combustion and PAH formation chemistry used a detailed chemistry mechanism by Narayanaswamy et al. [41] extended from Blanquart et al. [42]. The walls are specified to be adiabatic for all cases in this study.

A bivariate distribution with volume and surface area as internal coordinates is used to track the soot population balance equation [24]. Rather than solve explicitly for the evolution of this size distribution, only a finite set of moments (Eq. 2) is considered.

$$M_{x,y} = \int V^x A^y N d\zeta, \tag{2}$$

where x and y are the order of the moments in volume V and surface area A, respectively. N is the number density function described in terms of $\zeta = \{V, A\}$ and $d\zeta$ is $dAdV$. The set of moments used in this study are M_{00}, M_{10}, M_{01} and the weight of the delta function for the nucleated particles, N_0, for a total of four soot-related scalars transported. The transport equation for these moments is written in Eq. 3 where $S^M_{x,y}$ represents the moment source terms for nucleation from PAH dimers [43], condensation of PAH, particle coagulation (both coalescence and aggregation), surface growth by acetylene addition, and particle oxidation and fragmentation by oxidizing species. For brevity, the moment source terms are not explicitly written here but the reader is referred to [19, 24] for further details. u^* represents the total velocity, taking into account the difference between convective and thermophoretic velocities. Molecular diffusion is assumed to be negligible in this study. The HMOM approach [19] is used to solve the bivariate population balance equation.

$$\frac{\partial M_{x,y}}{\partial t} + \frac{\partial u^* M_{x,y}}{\partial x_j} = S^M_{x,y}, \tag{3}$$

The LES equations for soot moments and scalar fields are implemented in OpenFOAM [44], an operator-based C++ code for solving partial differential equations, which has been applied to a number of combustion systems [45–47]. However, the baseline codebase had to be substantially modified to ensure accurate evolution of the LES equations. Due to the low speeds within the combustor, a low-Mach number assumption is used, which requires solution of a pressure Poisson equation at each time-step [48]. It decouples the influence of pressure on the energy field. In the original solver, when primary variables such as mass and momentum are conserved, derived quantities such as kinetic energy may not be conserved in the limit of zero viscosity because it is not evolving according to a conservation equation that is solved. In structured-grid solvers that use staggered positioning of velocity and pressure variables, secondary conservation can be ensured by specific choice of divergence and gradient operators [7, 49, 50]. In fully unstructured mesh solvers, such as the one used here, a collocated variable approach is used, which prevents exact secondary conservation of kinetic energy. Minimally dissipative schemes are sought in order to reduce the effect of kinetic energy loss on flow evolution. Here, the variable density scheme of Morinishi [51] is used. The fluxes at the cell faces are computed using a second-order interpolation scheme. The governing equations are solved using a semi-implicit approximation that is second-order in time. This approach directly relates energy conservation to temporal convergence of the numerical scheme. To ensure second-order accuracy, a PISO (pressure-implicit second order) scheme is used [52] with at least two inner iterations. These specifications were found to reduce numerical dissipation [46]. This variable density solver, umFlameletFoam [46, 47, 53] is used for all the simulations discussed below and more details can be found in [54].

The flamelet library was constructed separately for each pressure, and soot source terms related to nucleation, surface growth, condensation, and oxidation were parameterized in terms of the rate coefficients and stored [39]. The progress variable source term scales approximately as $P^{0.65}$ (P is defined as the pressure), while the dimer production rate, which is a direct indicator of soot nucleation rate, scales approximately as $P^{1.57}$. Other soot related source terms have nearly linear increase with pressure.

4. Results and Discussion

In this section, the simulation results for the various cases are discussed. First, the gas-phase flow field is described, followed by description of sooting process in the combustor. Then, gas-phase and soot statistics are compared with experimental results and cause of deviations discussed. Finally, sidejet and pressure effects on soot are analyzed.

4.1. Qualitative description of the swirling flow

To understand the overall flow structure in the combustor, instantaneous snapshots from the different simulations are discussed here. For the cases computed at 3 bar pressure with and without sidejets, the flow field information is shown in Figs. 2 and 3. Similar to rich-quench-lean designs for gas turbines, the combustion zone is aerodynamically stabilized by a swirling flow in the near-field of the injector nozzle (Fig. 2). This creates an inner recirculation zone (IRZ), characterized by negative axial velocities over the center flow injection plane, and an outer recirculation zone (ORZ), located between the shear-layers formed by the fuel injectors and the side walls. When sidejets are present (Fig. 3), strong cross-flow mixing is introduced, with the sidejets creating a disruption to the axial flow. The resultant recirculation zone in the middle of the combustor is much stronger compared to the case with no sidejets. In fact, the presence of the sidejets leads to a high velocity zone right next to the side walls, which further isolates the fluid within the IRZ. Similarly, there is a strong acceleration in the axial flow at the exit of the domain, where the constriction of the dump combustor combined with increased flow rate from the sidejets lead to an increase in outflow velocity. While the overall flow structure might look similar, these subtle variations due to the presence of the sidejet, combined with the associated increase in oxidizer mass flow into the combustor, will lead to substantial changes in species and soot profiles (discussed below).

Figure 4 shows the instantaneous mixture fraction and temperature plots for 3 bar cases. The swirling inflow significantly augments mixing between the fuel and oxidizer streams. In the case without sidejets, this leads to near uniform mixtures short distance from the inflow. However, there is significant fluctuation in the mixture fraction profile upstream. In particular, it was found that the jets tend to exhibit large scale unsteadiness. Since this jet motion affects soot formation, it is useful to discuss this in more detail. Figure 5 shows the instantaneous location of the fuel jet arm at different times. It is seen that during certain time instances, the jet is deflected towards the IRZ, while at other times, the jet is directed away towards the ORZ. This occurs primarily due to the unsteadiness of the recirculation zone itself, which both precesses in the azimuthal direction and undergoes significant size and shape changes throughout the simulation period. The net effect is the dislodging of rich fuel mixtures from the jet into the recirculation zone. Hence, there exists significantly rich fuel pockets for prolonged times inside the IRZ, where slow recirculating zone with relatively high temperatures and long residence time can promote soot formation.

In the presence of sidejets, the mixture fraction and temperature contours (Fig. 4) are more complex. A low temperature zone forms near the sidejet interaction region in the center of the combustor. Moreover, there are pronounced gradients in temperature between the shear layers that isolate the inner and outer recirculation zones and the core of the IRZ. This flow structure illustrates that the secondary oxidation air is not simply transported downstream but is predominantly entrained into the IRZ. In this case, strong temperature gradients persist towards the exit of the combustor. As a result, there exists a relatively low temperature (< 1000 K) region along the axial length of the combustor, while higher temperatures are found near the walls and the shear layers. This suggests a more diffusion-flame like structure as compared to a homogeneous premixed-flame type behavior for the case without sidejets.

Figures 6 and 7 show time-averaged velocity fields for all the cases considered. The prominent features in the axial profile include the negative velocity recirculation zones and the arms of the shear layer extending the entire axial distance of the combustor. Since the combustor is not cylindrical, there is variation in these profiles for different azimuthal angles, but the general trends hold. Of particular significance is the comparison between the 3 and 5 bar cases. As noted above, the two cases have identical inflow velocity conditions but differ in the fluid density and the Reynolds number of the flow. At 66% higher Reynolds number, the 5 bar case is more turbulent, which leads to a slightly modified IRZ with two symmetric lobes. With sidejets, the IRZ is more compact and centered near the sidejet interaction region at the center of the combustor for the higher pressure case. Tangential velocity profiles show the formation of an enclosure for the IRZ at 3 bar case with sidejet, while the enclosure does not exist at 5 bar.

Figure 8 shows time-averaged temperature profiles for all cases. Similar to the instantaneous images, the temperature field is nearly uniform downstream of the near-nozzle region, with symmetric mixing shown in the form of a V-shape near the nozzle. In the case with sidejets, this near-nozzle region is preserved, but temperature is reduced in the sidejet interaction region in the center of the combustor. Further, there are clear regions of temperature gradient along the axial distance of the combustor. This is reflected in the instantaneous images of temperature and mixture fraction shown above. Since the time-averaged and instantaneous profiles look similar, it can be concluded that the temperature gradients persist during the entire simulation, and are part of the flow features when sidejets are present.

The differences in the temperature distribution are created by changes in the mixture fraction field (Fig. 9). The comparisons between four cases show that there are clear differences between cases with and without sidejets, while the change in pressure only affects the distribution of mixture fraction in a more subtle manner. The 3 bar case shows a slightly richer field in the IRZ, in spite of having identical global equivalence ratios. This is due to large scale flow structure differences between the cases at different Reynolds numbers, deflecting more fuel rich pockets into the IRZ at 3 bar. It is seen that the case with sidejet leads to much lower mixture fraction values in the domain, specifically in the IRZ, due to higher oxidizer concentration. Further, the fuel jet is deflected more towards the wall in the sidejet case, leading to higher temperature in the shear layers.

4.2. Evolution of soot particles

Soot generation is inherently intermittent, leading to large variations in volume fraction with time (see discussion in [5, 55], and references within). As a result, instantaneous snapshots cannot reveal the full picture about the location of peak soot production. Figure 10 shows soot volume fraction contour with OH mass fraction and stoichiometric mixture fraction line. For this configuration that is far from extinction limits, the peak reaction rates for gas phase fuel oxidation occur near the stoichiometric line. As expected, soot is generated on the rich side, while OH concentration peaks on the lean side of this stoichiometric contour. It is important to recognize that even though the OH structure is linked to the stoichiometric contour directly through the flamelet table, soot generation is only indirectly affected through the source terms in the population balance (moment) equations. Further, there is almost no soot leakage to the lean side in the sidejet case, indicating complete oxidation of the particulate phase.

In comparing with instantaneous velocity and mixture fraction profiles (Figs. 2, 3 and 4), it is seen that soot generation occurs in small fuel-rich pockets located near the shear layers generated by the fuel and oxidizer jets entering the domain. Due to the slow kinetics associated with soot, significant volume fraction is only observed several jet diameters downstream of the fuel nozzle. In particular, much of soot formation is confined to the arms of the jet. Time sequences (not shown here) confirm that soot production is dominated by this shear region and the soot number density, which is a marker for nucleation, shows peak values also along this shear layer, with significant drop further downstream due to combined effects of agglomeration and oxidation. Comparing the cases with and without sidejets in Fig. 10, the simulations show that the presence of the sidejet reduces soot formation in the near-nozzle region, especially in the shear layer formed between the IRZ and the fuel/oxidizer jets. Further, sidejets also increase oxidation of soot with increased OH mass fraction downstream.

The intermittency of soot formation can be viewed through snapshots rather than individual images. Figure 11 shows soot volume fraction images separated by 2 ms in time. It is seen that soot is distributed sparsely in the domain, with small patches of high soot concentration. Experiments show similar sparse soot presence, albeit with higher soot concentrations in some cases [32]. The instantaneous soot volume fraction contours further verify that soot near the bottom of the IRZ occurs through intermittent patches. As a result, even though the fluid from the inlet reaches combustor exit in roughly 12.5 ms, the soot motion within the IRZ is comparatively slower, and will require much longer simulation and averaging time in order to obtain converged statistics (See Appendix B for more details).

This intermittency is driven by the turbulent fluctuations of the gas-phase composition, and the slower response of the soot formation processes. In particular, it is seen that the flapping motion from the fuel jet in Fig. 5 shows mixture fraction contours near the fuel jet inlet with the jet arm at extreme locations in the radial direction. At certain times, the jet breaks down immediately after entering the combustor, leading to fuel-rich pockets that are entrained by the recirculation zone. This shearing motion is amplified by the highly unsteady transverse motions of the recirculation zone. The jet-flapping is the main source of intermittency in this combustor. Unlike intermittency due to small scales [56], soot intermittency in such gas turbines is driven by these large scale hydrodynamic motions. The sporadic soot generation is the result of such large scale motions introducing fluid trajectories that pass through soot-favored regions in composition space. Therefore, capturing unsteadiness especially in the inlet condition is important in soot prediction of this configuration.

4.3. Validation against experimental results

4.3.1. Gas phase statistics

Since the soot phase exhibits slow temporal dynamics, statistics of the flow have to be obtained over long averaging times. A discussion of the convergence of these statistical features is provided in Appendix B. Further, due to the highly chaotic and unsteady nature of the flow, grid convergence also needs to be established. In theory, grid-filtered LES cannot be grid converged, since any mesh refinement automatically implies a change in filter width [57]. However, statistics of large scale properties generally converge with resolution as high-gradient regions such as shear layers are better captured. Hence, grid convergence should be used more as a qualitative metric of the reliability of the results, rather than a strict reduction of numerical truncation errors [58–60]. Such a grid convergence study is presented in Appendix A.

Figures 12 to 14 show comparisons of gas-phase velocity statistics with experimental data. Note that PIV-based velocity information is available only for the 3 bar case and not all positions are shown for conciseness. Comparisons are only shown for selected locations most pertinent to capturing the mixing region, high velocity shear layer, and recirculation zone. These results show that the simulations are extremely adept at capturing the flow structure, including the details of the recirculation zone and the tangential velocity components. Moreover, Fig. 14 shows that Root-Mean-Square (RMS) velocity is captured accurately as well. There are no experimental data for comparison of RMS velocity for 3 bar case without sidejet but flow fluctuations are captured well in the more turbulent case with sidejet injection, especially at the sidejet interaction region (80 mm). It is important to recognize that, given the complexity of the flow field and the highly unsteady nature of the turbulent system, such good comparisons throughout the flow path are encouraging. The good prediction of RMS velocity components further shows that the use of the refined grid and the reduced-dissipation numerical approach is well-suited for such complex geometries.

Figure 15 shows the mean centerline temperature profiles from experiments and simulations, while Fig. 16 shows comparisons for mean radial temperature profiles at selected axial locations (and only at 3 bar condition). In general, the simulation profiles are consistent with the experimental results. For the cases with sidejet for both pressures, the model captures the trend but underpredicts the temperature at the centerline. More specifically, the dip in temperature near the sidejet interaction region is captured well in the axial and radial profiles, respectively. The temperature profile peaks in the near-nozzle region, at the base of the recirculation zone where stoichiometric conditions are reached, and decreases (for sidejets) or stays nearly uniform (without sidejets) downstream. Agreement for the radial profiles is satisfying, with reduction in temperature at downstream locations captured well. The experimental data does have some limitations, including the inability to get near-wall readings at the time of this simulation study. Further, it is important to note that the width of measured experimental statistics are relatively large, which makes a more refined comparison with simulations not very meaningful. In complex geometries, the lack of fidelity of experiments is well-appreciated, and these results are a demonstration of such challenges.

4.3.2. Soot statistics

Figures 17 and 18 show comparisons of time-averaged LES with experimental soot volume fraction fields for 3 and 5 bar cases respectively. As expected, the higher pressure case contains higher soot volume fractions, especially in the shear layers close to the side walls. The LES computation captures this trend, providing basic verification of the pressure dependence of the chemical source terms. However, the soot volume fraction for 5 bar case is underpredicted by about a factor of 4. Without the sidejets in the 3 bar case, experiments show peak soot concentrations in the IRZ. The simulations show soot locations predominantly in the shear layers, which is consistent with the instantaneous snapshots in Sec. 4.2. The presence of the sidejets leads to soot being confined to the shear layers in the experiments, which is consistent with the LES results.

Figures 19 and 20 show radial plots of experimental and LES results, which provide a more quantitative comparison. As seen, the simulations underpredict experimental data by an order of magnitude, depending on the location and pressure condition. At 5 bar pressure, the model predicts accurately the soot locations but consistently underpredicts soot volume by about a factor of 5. Another prominent deviation is the consistent underprediction of soot volume fraction downstream of the combustor. Soot oxidation rate or OH mass fraction could have been overpredicted to cause such a deviation. As seen in the contour plots (Figs. 17 and 18), soot formation in the recirculation zone is underpredicted in the models, which leads to the lack of a pronounced peak as in the experimental profile at 20 mm axial position. The trajectories of the soot pockets in the simulations do not promote soot mass addition in the IRZ. The presence of the sidejet diminishes this peak in the 3 bar case in the experiment, essentially due to increased oxidation of the entrained fluid, although the reason as to why the soot arm was not shortened by the sidejet at 3 bar when the 5 bar case shows such behavior is still unknown. Compared to other simulation works on the 3 bar case with sidejet [34, 35], the current model predicts the spatial and magnitude of soot volume fraction more accurately. Using a semi-empirical, PAH-based soot model, Eberle et al. [34] overpredicted the soot volume fraction in the shear layer and underpredicted the soot volume fraction at the central region above the inlet. Simulations with moment based models (current study and Wick et al. [35]) predict soot at the same location above the inlet. The one similarity across different models is the high oxidation rate above 70 mm in the combustor, leading to underprediction of soot in the downstream region. In the 5 bar case, the model predicts essentially an order of magnitude lower soot volume fraction at the zone right above the nozzle compared to the experiment. This could be caused by a lack of information on the velocity boundary conditions for the 5 bar cases that could help elucidate the overall flow structure of the case.

While these results show qualitative agreement, there are still considerable differences. In particular, the switch from IRZ-based soot formation to shear-layer formation that is observed in experiments without and with sidejets is not fully captured by the simulations. In order to determine the possible reasons for these deviations, it is important to discuss these results in the context of prior studies. As briefly mentioned in Section 1, prior results using the models described here have provided disparate conclusions. Simulations of jet flames have generally underpredicted soot volume fractions [21, 22, 25], while bluff-body type recirculation flows have yielded better agreement with simulations [26]. Partly, this is due to the nature of the models that are active. In jet flames, PAH-based condensation was found to be responsible for much of the soot growth, while in recirculation-dominated flows, growth through acetylene addition is of more importance [26].

To understand the relative contributions of different physical processes, the source term contributions for the volume moment is plotted in Fig. 21 for the 5 bar case with and without sidejets. The dominant soot mass generation term is due to acetylene-based surface growth, which is spatially located adjacent to the peak oxidation zone, and separated by the stoichiometric contour line. Unlike bluff-body stabilized flames, there is no clear regions where PAH condensation based growth or nucleation is dominant. In the presence of sidejets, all generation terms are significantly suppressed, mainly due to the entrainment of oxidation air into the IRZ. Regardless, acetylene-based growth is still the dominant contributor to soot volume fraction.

Given this surface-growth based soot formation, a better prediction of soot is to be expected given results from prior studies. We attribute the deviation from experiments to small errors in velocity and mixture fraction fields. It is known that acetylene concentrations are not sensitive to small-scale dissipation rate fluctuations [56]. Hence, these discrepancies can arise from deficiencies in the soot models themselves and the inability to predict flow fields with high precision. For instance, in regions where the RMS velocity comparisons are good, soot predictions are also equally better. Other studies have also shown similar sensitivity to the flow field [35]. In other words, the level of accuracy with which the flow field needs to be captured is significantly higher for predicting soot as compared to gas-phase species.

While the average source terms shown above provide the dominant mechanisms, their relative importance also depend on the particular trajectories that soot particle take inside the combustor. To obtain this information, a Lagrangian approach is used to follow particle-like trajectories during the LES calculation. An ensemble of notional particles is released into the domain through the fuel injection ports. In this case, roughly 1000 particles are followed. The injection point is consistent across all four cases and is located directly above the fuel port as shown in Fig. 10. The source of the injection point is a sphere of diameter 0.5 mm with the particle positioned at the surface of the sphere. Particles are tracked for a total of 75 ms, sufficiently long to determine soot mass addition behavior. The notional particles are advanced in space using the local fluid velocity. At each time-step, the gas-phase properties and soot source terms associated with the local Eulerian soot field are stored. Time along the particle trajectory is regarded as residence time in the chamber and only the axial position of the particle is of interest whereby any particle having axial position $Z < 40$ mm after a residence time of 0.01 s is regarded as being in the recirculation zone.

These trajectories can be classified into three dominant classes:: (i) Particle Type 1, where particles are convected downstream following the flow field close to the wall and subsequently exit rapidly through the outlet, (ii) Particle Type 2, particles that remain in the recirculation zone upstream, and (iii) Particle Type 3, particles that are entrained into the IRZ at a downstream location and convected back upstream.

Figure 22 shows mass source terms for each kind of particle in the combustor. The intermittency of soot generation can be readily seen from the fluctuating soot source terms encountered along the particle trajectory. Type 1 particles experience high soot production and oxidation fields, but remain inside the combustor only for a short time. Such particles are expected to travel along the arms of the shear layer, and are subject to soot evolution processes akin to a non-premixed jet. Type 2 and 3 particles undergo weaker but multiple soot mass addition events, indicating that they pass through relatively fuel-rich regions of the flow multiple times. Even if the source terms are not very high, the long residence times provide the means for sufficient soot mass addition.

In order to further understand the characteristics of different soot paths, the conditional mean trajectories (based on particle type) of the notional particles in mixture fraction and progress variable space are plotted in Fig. 23. It is seen that the Type 1 particles start from the rich side of the jet, and traverse through the high temperature region towards the lean side. On the other hand, Type 3 particles start from the rich side and move to richer parts of the jet, and pass through similar gas-phase compositions multiple times, mostly at the downstream region of the IRZ. Type 2 particles provide the transition from 1 to 3, with slight motion towards the rich side before moving back towards the lean region of the combustor. The percentage of each of these types of particles are highlighted in Table 2. It can be seen that Type 1 particles dominate in this combustor, regardless of the operating condition considered. Further, the percentage of Type 1 particles increase as pressure increases. A similar trend is noticed when sidejets are introduced at any given pressure. Hence, air injection not only reduces the global equivalence ratio, but also changes the hydrodynamic structure of soot generation.

It is apparent that the higher pressure case contains higher soot concentrations than the lower pressure case, although the regions of soot formation are similar. Further, the peak soot levels are higher in the 5 bar case compared to the 3 bar case.

The differences in the soot formation process for the 3 and 5 bar cases can be diagnosed using the Lagrangian trajectories as well. Figure 24 shows the scatter plot of Lagrangian particle locations in phase space superimposed on surface growth rate, for the two different pressure cases and without sidejet injection. It can be seen that in the 3 bar case, the trajectories are such that all particle types traverse to regions of high soot surface growth. On the other hand, the Type 2 and 3 particles in the 5 bar case only rarely reach the high soot production regions, and are in general traversing fuel-lean parts of the phase-space. More importantly, the Type 1 particles in the 5 bar case traverse a greater distance along low temperature zones, as shown by the cluster of data points near the low progress variable region. As a result, even though the soot growth rate is considerably increased due to the pressure (roughly a factor of 2), the lack of sufficient number of fluid trajectories in such regions lead to a suppressed increase in soot formation. Hence, the conventional pressure scaling of $P^{1.7}$ [36] is not directly translatable to turbulent combustor. This suggests that there exists a separate hydrodynamic scaling, separated from the kinetic-controlled pressure scaling, which alters the rate of increase of soot with pressure.

5. Conclusions

LES of soot formation in realistic gas turbine combustors was performed for four different cases, including two pressure conditions, with and without sidejets. From a computational perspective, it was found that soot statistics have to be converged over time-scales much longer than that for the gas-phase flow field. This is predominantly due to the presence of low-frequency unsteady events that generate large soot volume fractions. In other words, if the joint-probability of all states of the combustor are considered, the tails of this distribution influence soot mass inside the system.

The simulations predict gas-phase statistics such as flow-field information quite accurately. While the comparisons with temperature profiles could be better, simulation data is still generally within one sigma standard deviation of experimental measurements. Soot statistics show some interesting trends. First, the spatial structure of soot formation is nearly well-captured, although pockets of high soot mass in the IRZ are not present in the simulations for the 3 bar case without sidejet. The effect of sidejets is also captured, including the reduction in soot concentration as well as the decrease of soot volume in the shear layer downstream. Second, the quantitative comparisons show that soot is underpredicted, but the values are much better for this configuration compared to simulations using identical models but for canonical jet flames.

These simulations reveal two key features of soot formation in a gas turbine environment. Unlike in canonical jet flames, soot mass addition is driven by acetylene-based growth, which is less sensitive to local strain-rates. Further, swirling flows at high Reynolds numbers exhibit inherent unsteadiness that can lead to sporadic (intermittent) fluid trajectories that promote soot growth. In the configuration studied here, such generation is through the side-to-side motion of the fuel jet, which results in fuel-rich pockets being lobbed-off and transported to low velocity, soot-promoting regions. Interestingly, such intermittency is observed both in the experiments utilized here, as well as in other studies of soot formation [26, 55].

From lagrangian particle trajectory analysis, it is revealed that without sidejets, a higher percentage of notional particles are entrained into the IRZ (Particle Type 3) at 3 bar pressure. These particles in the recirculation zone experience highly intermittent soot production and oxidation source terms with large residence times. Increasing the pressure changes the hydrodynamic field and behavior of particle trajectories, with less particles being entrained into the IRZ. Thus, at different pressures and flow field, these particles traject a different mixture fraction-progress variable phase space, leading to differences in soot mass addition.

Such unsteady-motion driven soot formation adds a hydrodynamic mode to the scaling laws for soot formation associated with pressure changes. In laminar ethylene flames, $P^{1.7}$ has been observed, with some variation in the exponent based on the metric used. While there is an increase in soot concentration in the gas turbine combustor as well, this increase is also linked to the change in unsteadiness with pressure. In particular, if an increase in pressure (and hence, Reynolds number) reduces the intermittent jet flapping, it might actually lead to a reduction of overall soot formation. Such hydrodynamic causation cannot be observed even in canonical turbulent flames, since large scale unsteadiness is linked directly to the geometry and is not universal in nature. Similar to thermoacoustic instabilities, there is a need to understand the role of such large-scale driven features on soot formation. Perhaps, variations in the configuration including changes to the inflow can be used to assess this feature more systematically. Such investigations are left for future studies.

Acknowledgements

This study was partially funded by NASA through the project number NNX16AP90A, with Dr. Jeff Moder as the program monitor. KPG was supported by European project Fuel Injector Research for Sustainable Transport (Contract No. 265848).

References

[1] A. E. Karatas, Ö. L. Gülder, Soot formation in high pressure laminar diffusion flames, Prog. Energ. Combust. Sci. 38 (2012) 818–845.

[2] H. Wang, Formation of nascent soot and other condensed-phase materials in flames, Proc. Combust. Inst. 33 (2011) 41–67.

[3] M. E. Mueller, Large eddy simulation of soot evolution in turbulent reacting flows, Ph.D. thesis, Stanford University, 2012.

[4] M. R. J. Charest, H. I. Joo, Ö. L. Gülder, C. P. T. Groth, Experimental and numerical study of soot formation in laminar ethylene diffusion flames at elevated pressures from 10 to 35 atm, Proc. Combust. Inst. 33 (2011) 549–557.

[5] V. Raman, R. O. Fox, Modeling of fine-particle formation in turbulent flames, Ann. Rev. Fluid Mech. 48 (2016) 159–190.

[6] H. Pitsch, Large-eddy simulation of turbulent combustion, Ann. Rev. Fluid Mech. 38 (2006) 453–482.

[7] K. Mahesh, G. Constantinescu, P. Moin, A numerical method for large-eddy simulation in complex geometries, J. Comput. Phys. 197 (2004) 215–240.

[8] M. E. Mueller, H. Pitsch, Large eddy simulation of soot evolution in an aircraft combustor, Phys. Fluids 25 (2013) 110812.

[9] T. Poinsot, D. Veynante, Theoretical and Numerical Combustion, R. T. Edwards, Philadelphia, USA, 2001.

[10] F. Di Mare, W. P. Jones, K. R. Menzies, Large eddy simulation of a model gas turbine combustor, Combust. Flame 137 (2004) 278–294.

[11] H. Koo, M. Hassanaly, V. Raman, M. E. Mueller, K. P. Geigle, Large-eddy simulation of soot formation in a model gas turbine combustor, J. Eng. Gas Turbines and Power 139 (2017) 031503.

[12] H. Koo, V. Raman, M. E. Mueller, K. P. Geigle, Large-eddy simulation of a turbulent sooting flame in a swirling combustor, in: 53rd AIAA Aerospace Sciences Meeting, 2015-0167.

[13] H. Koo, V. Raman, M. E. Mueller, K.-P. Geigle, LES of a sooting flame in a pressurized swirl combustor, in: 54th AIAA Aerospace Sciences Meeting, 2016-2123.

[14] F. Ham, S. Apte, G. Iaccarino, X. Wu, M. Herrmann, G. Constantinescu, K. Mahesh, P. Moin, Unstructured LES of reacting multiphase flows in realistics gas turbine combustors, in: CTR Annual Research Briefs, Center for Turbulence Research, CTR, Stanford University, pp. 139–160.

[15] M. Frenklach, H. Wang, Detailed modeling of soot particle nucleation and growth, Symp. (Int.) Combust. 23 (1991) 1559–1566.

[16] H. Wang, M. Frenklach, A detailed kinetic modeling study of aromatics formation in laminar premixed acetylene and ethylene flames, Combust. Flame 110 (1997) 173–221.

[17] M. Frenklach, S. J. Harris, Aerosol dynamics modeling using the method of moments, J. Colloid Interface Sci 118 (1987) 252–261.

[18] D. L. Marchisio, R. O. Fox, Solution of population balance equations using the direct quadrature method of moments, J. Aerosol Sci 36 (2005) 43–73.

[19] M. E. Mueller, G. Blanquart, H. Pitsch, Hybrid method of moments for modeling soot formation and growth, Combust. Flame 156 (2009) 1143–1155.

[20] R. Lindstedt, S. Louloudi, Joint-scalar transported pdf modeling of soot formation and oxidation, Proc. Combust. Inst. 30 (2005) 775–783.

[21] P. Donde, V. Raman, M. E. Mueller, H. Pitsch, LES/PDF based modeling of soot-turbulence interactions in turbulent flames, Proc. Combust. Inst. 34 (2013) 1183–1192.

[22] Y. Xuan, G. Blanquart, Effects of aromatic chemistry-turbulence interactions on soot formation in a turbulent non-premixed flame, Proc. Combust. Inst. 35 (2015) 1911–1919.

[23] C. D. Pierce, P. Moin, Progress-variable approach for large-eddy simulation of non-premixed turbulent combustion, J. Fluid Mech 504 (2004) 73–97.

[24] M. E. Mueller, G. Blanquart, H. Pitsch, A joint volume-surface model of soot aggregation with the method of moments, Proc. Combust. Inst. 32 (2009) 785–792.

[25] International Sooting Flame Workshop 2, https://www.adelaide.edu.au/cet/isfworkshop, 2014 , Accessed: September, 5th, 2017.

[26] M. E. Mueller, Q. N. Chan, N. H. Qamar, B. B. Dally, H. Pitsch, Z. T. Alwahabi, G. J. Nathan, Experimental and computational study of soot evolution in a turbulent nonpremixed bluff body ethylene flame, Combust. Flame 160 (2013) 1298–1309.

[27] H. El-Asrag, S. Menon, Large eddy simulation of soot formation in a turbulent non-premixed jet flame, Combust. Flame 156 (2009) 385–395.

[28] V. Raman, H. Pitsch, A consistent LES/filtered-density function formulation for the simulation of turbulent flames with detailed chemistry, Proc. Combust. Inst. 31 (2006) 1711–1719.

[29] A. Kempf, R. P. Lindstedt, J. Janicka, Large-eddy simulation of bluff-body stabilized nonpremixed flame, Combust. Flame 144 (2006) 170–189.

[30] M. E. Mueller, V. Raman, Effects of turbulent combustion modeling errors on soot evolution in a turbulent nonpremixed jet flame, Combust. Flame 161 (2014) 1842–1848.

[31] K. M. Leung, R. P. Lindstedt, W. Jones, A simplified reaction mechanism for soot formation in nonpremixed flames, Combust. Flame 87 (1991) 289–305.

[32] K. P. Geigle, R. Hadef, W. Meier, Soot formation and flame characterization of an aero-engine model combustor burning ethylene at elevated pressure, J. Eng. Gas Turbines and Power 136 (2014) 021505.

[33] C. Eberle, P. Gerlinger, K. P. Geigle, M. Aigner, Soot predictions in an aero-engine model combustor at elevated pressure using URANS and finite-rate chemistry, in: 50th AIAA/ASME/SAE/ASEE Joint Propulsion Conference, AIAA 2014-3472.

[34] C. Eberle, P. Gerlinger, K. P. Geigle, M. Aigner, Numerical investigation of transient soot evolution processes in an aero-engine model combustor, Combust. Sci. Technol. 187 (2015) 1841–1866.

[35] A. Wick, F. Priesack, H. Pitsch, Large-eddy simulation and detailed modeling of soot evolution in a model aero engine combustor, in: ASME Turbo Expo 2017: Turbomachinery Technical Conference and Exposition, GT2017-63293.

[36] L. L. McCrain, W. L. Roberts, Measurements of the soot volume field in laminar diffusion flames at elevated pressures, Combust. Flame 140 (2005) 60–69.

[37] K. P. Geigle, M. Köhler, W. OLoughlin, W. Meier, Investigation of soot formation in pressurized swirl flames by laser measurements of temperature, flame structures and soot concentrations, Proc. Combust. Inst. 35 (2015) 3373–3380.

[38] K. P. Geigle, R. Hadef, M. Stöhr, W. Meier, Flow field characterization of pressurized sooting swirl flames and relation to soot distributions, Proc. Combust. Inst. 36 (2017) 3917–3924.

[39] M. E. Mueller, H. Pitsch, LES models for sooting turbulent nonpremixed flames, Combust. Flame 159 (2012) 2166–2180.

[40] V. Raman, H. Pitsch, Large-eddy simulation of a bluff-body-stabilized non-premixed flame using a recursive filter-refinement procedure, Combust. Flame 142 (2005) 329–347.

[41] K. Narayanaswamy, G. Blanquart, H. Pitsch, A consistent chemical mechanism for oxidation of substituted aromatic species, Combust. Flame 157 (2010) 1879–1898.

[42] G. Blanquart, P. Pepiot-Desjardins, H. Pitsch, Chemical mechanism for high temperature combustion of engine relevant fuels with emphasis on soot precursors, Combust. Flame 156 (2009) 588–607.

[43] G. Blanquart, H. Pitsch, Combustion Generated Fine Carbonaceous Particles, Karlsruhe University Press, (2009) 437-463.

[44] The Open Source CFD Toolbox, 2017. OpenCFD Inc. http://www.openfoam.com.

[45] M. Chapuis, E. Fedina, C. Fureby, K. Hannemann, S. Karl, J. M. Schramm, A computational study of the HyShot II combustor performance, Proc. Combust. Inst. 34 (2013) 2101–2109.

[46] H. Koo, M. Hassanaly, V. Raman, M. E. Mueller, K. P. Geigle, Large-eddy simulation of soot formation in a model gas turbine combustor, in: ASME Turbo Expo 2016, GT2016-57952.

[47] C. Lietz, C. Heye, V. Raman, D. Blunck, Flame stability analysis in an ultra compact combustor using large-eddy simulation, in: 52nd AIAA Aerospace Science Meeting, AIAA 2014-1022.

[48] J. Kim, P. Moin, R. D. Moser, Turbulence statistics in fully developed channel flow at low Reynolds number, J. Fluid Mech 177 (1987) 133–166.

[49] O. Desjardins, V. Moureau, H. Pitsch, An accurate conservative level set/ghost fluid method for simulating turbulent atomization, J. Comput. Phys. 227 (2008) 8395–8416.

[50] J. H. Ferziger, M. Peric, Computational Methods for Fluid Dynamics, Springer, 3rd edition, 2002.

[51] Y. Morinishi, T. S. Lund, O. V. Vasilyev, P. Moin, Fully conservative higher order finite difference schemes for incompressible flow, J. Comput. Phys. 143 (1998) 90–124.

[52] R. I. Issa, Solution of the implicitly discretised fluid flow equations by operator-splitting, J. Comput. Phys. 62 (1985) 40–65.

[53] C. Lietz, V. Raman, Large eddy simulation of flame flashback in swirling premixed CH_4/H_2-air flames, in: 53rd AIAA Aerospace Science Meeting, AIAA 2015-0844.

[54] M. Hassanaly, H. Koo, C. F. Lietz, S. T. Chong, V. Raman, A minimally-dissipative low-Mach number solver for complex reacting flows in OpenFOAM, Computer and Fluids 162 (2018) 11–25.

[55] N. Qamar, Z. Alwahabi, Q. Chan, G. Nathan, D. Roekaerts, K. King, Soot volume fraction in a piloted turbulent jet non-premixed flame of natural gas, Combust. Flame 156 (2009) 1339–1347.

[56] A. Attili, F. Bisetti, M. E. Mueller, H. Pitsch, Formation, growth, and transport of soot in a three-dimensional turbulent non-premixed jet flame, Combust. Flame 171 (2014) 1849–1865.

[57] S. B. Pope, Ten questions concerning the large-eddy simulation of turbulent flows, New Journal of Physics 6 (2004) 35.

[58] C. M. Kaul, V. Raman, G. Balarac, H. Pitsch, Numerical errors in the computation of subfilter scalar variance in large eddy simulations, Phys. Fluids 21 (2009) 055102.

[59] C. M. Kaul, V. Raman, A posteriori analysis of numerical errors in subfilter scalar variance modeling for large eddy simulation, Phys. Fluids 23 (2011) 035102.

[60] C. Heye, C. M. Kaul, V. Raman, Analysis of scalar variance modeling for large eddy simulation of combustion using explicit filtering, in: Proceedings of Turbulence and Shear Flow Phenomena Conferences 2011.

[61] S. B. Pope, Turbulent Flows, IOP Publishing, 2001.

Appendix

A. Grid Convergence Study

The computational mesh used for this study is shown in Fig. 25. A fully unstructured mesh with tetrahedral cells is used. Near the walls, five layers of prism-shaped pentahedrons are used to capture the boundary layers. The mesh is refined close to the jet inlet but is coarser further downstream where the gradients are smaller. Three mesh resolutions are tested: 6, 12, and 77 million mesh. On the denser mesh, a refined zone is added close to the inlet where flow experiences high shear from multiple inlet ports. The mesh quality is assessed using Pope's criterion [57, 61] and plotted in Fig. 25. While further mesh resolution might be needed along the central air passage below the fuel nozzle, the denser 12 million mesh significantly improves the resolution in the primary flame and soot nucleating region. Further refinement to 77 million mesh did not produce significant change in results. For this study, the 12 million cell case is used.

Velocity and soot volume fraction convergence for the 3 different meshes of increasing resolution are also seen in Figs. 26 and 27. From 6 mil to 12 mil mesh, it is clear that the soot volume fraction reduces by a factor of 2. This decrease is attributed to the change in numerical dissipation. With a higher resolution, the dissipation rate captured is higher, which reduces the PAH concentrations that cause soot mass addition.

The LES computations were performed on 1024 cores, with each simulation starting from a non-reacting steady state solution and requiring roughly

100 wall-clock hours to reach sufficient number of flow-through times for averaging and further analysis. Statistics were collected for roughly 20 flow-through times, computed based on the mean axial velocity and length of the domain. It should be noted that this averaging time is sufficient for gas-phase statistics, such as those related to velocity and thermochemical state, but soot fields take much longer to converge as will be shown in the next section.

B. Temporal convergence of soot statistics

Since soot evolution occurs over longer time scales compared to gas-phase oxidation of fuel, temporal convergence of soot statistics needs to be determined. For this purpose, simulations were carried over a 200 ms time-period, which is approximately equivalent to 8 flow-through times, estimated based on the inflow velocity and the axial length of the combustor. Figure 28 show ensemble averages over progressively longer simulation times. It is seen that although gas-phase statistics converge within 100 ms, the soot statistics take much longer, and appear statistically converged only after 135 ms.

In Fig. 29 and Fig. 30, radial profiles of soot volume fraction converged using different averaging times are plotted. It is seen that soot volume fraction increases in certain regions of the combustor with averaging time, especially over the central air flow region (at the center of the IRZ), where fluid velocities are relatively low. As averaging time increased from 103 ms to 172 ms in Fig. 28, it is found that the soot volume fraction field becomes more compact (radially), as expected of a stabilized flame and flow field where nucleation at the middle of the chamber accounts for the soot volume fraction increase in the region.

Pressure (bar)	$Q_{air,c}$ (slpm)	$Re_{air,c}$	$Q_{air,r}$ (slpm)	$Re_{air,r}$	Q_{fuel} (slpm)	Q_{oxi} (slpm)	Re_{tot}	ϕ_{global}
3	140.8	17,800	328.5	16,500	39.3	0	40,800	1.2
3	140.8	17,800	328.5	16,500	39.3	187.4	40,800	0.86
5	234.2	29,600	546.2	27,500	65.4	0	67,800	1.2
5	234.2	29,600	546.2	27,500	65.4	312.1	67,800	0.86

Table 1: Flow parameters and operating conditions for the simulated cases. *air,c* and *air,r* indicate central air and ring air respectively. *oxi* indicates the dilution jet air. ϕ_{global} indicates global equivalence ratio. Standard flow rates are referenced to 1.013 bar and 273 K. ρ_{air} and ρ_{fuel} are 1.18 kg/m^3 and 1.15 kg/m^3 respectively at 1 bar inlet operating conditions. [32]

Case	Particle Type 1 (%)	Particle Type 2 (%)	Particle Type 3 (%)
3 bar, No sidejet	76.3	21.3	2.4
3 bar, Sidejet	78.6	21.1	0.3
5 bar, No sidejet	83.1	16.5	0.4
5 bar, Sidejet	84.8	14.9	0.3

Table 2: Percentage of particle types by trajectory illustrated in Fig 22.

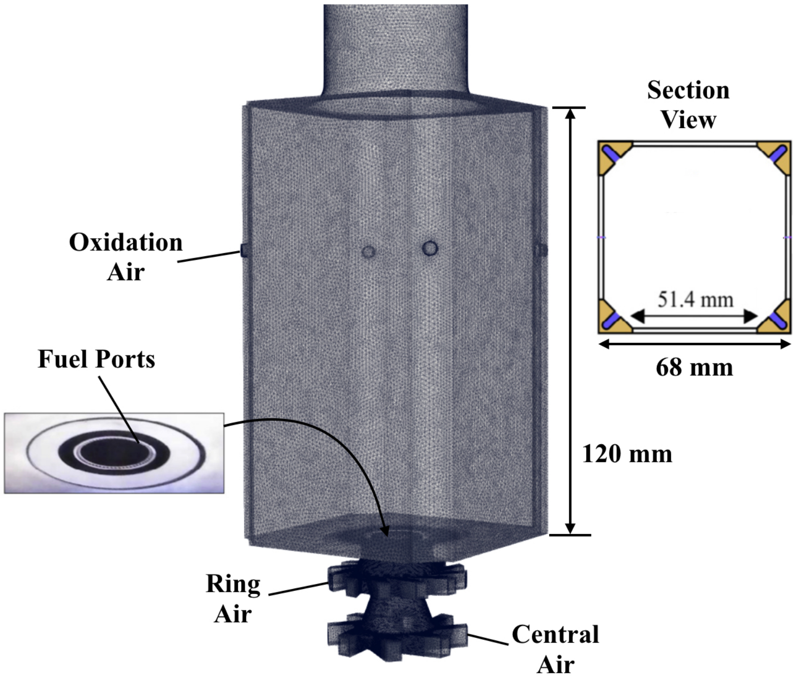

Figure 1: Combustor geometry and computational unstructured mesh (12 million cells), inlet nozzle details, and planar cross sections at the height of secondary oxidation air injectors.

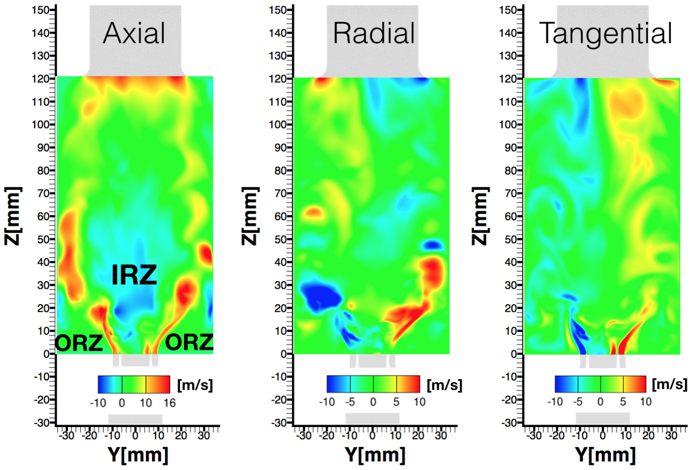

Figure 2: Instantaneous velocity contours for 3 bar case without sidejet. Locations of inner recirculation zone (IRZ) and outer recirculation zone (ORZ) are specified.

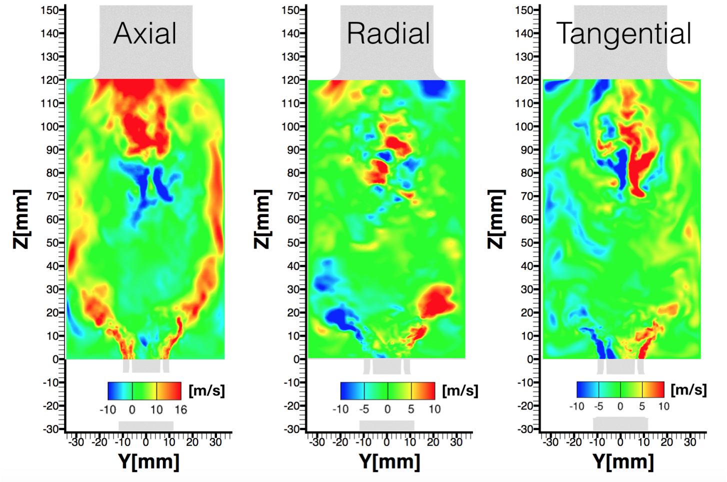

Figure 3: Instantaneous velocity contours for 3 bar case with sidejet.

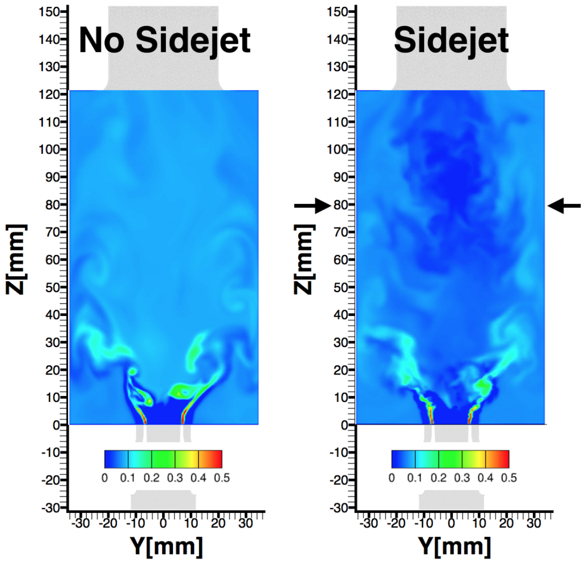

(a) Mixture Fraction

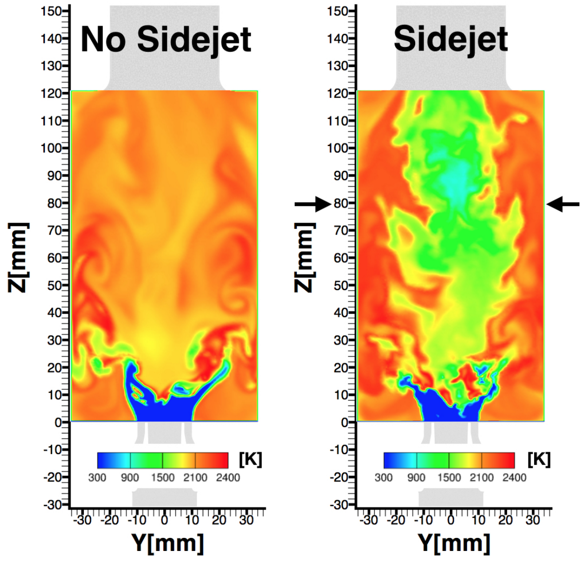

(b) Temperature

Figure 4: Instantaneous mixture fraction and temperature contour comparisons for 3 bar case. Arrows indicate location where dilution jet is injected.

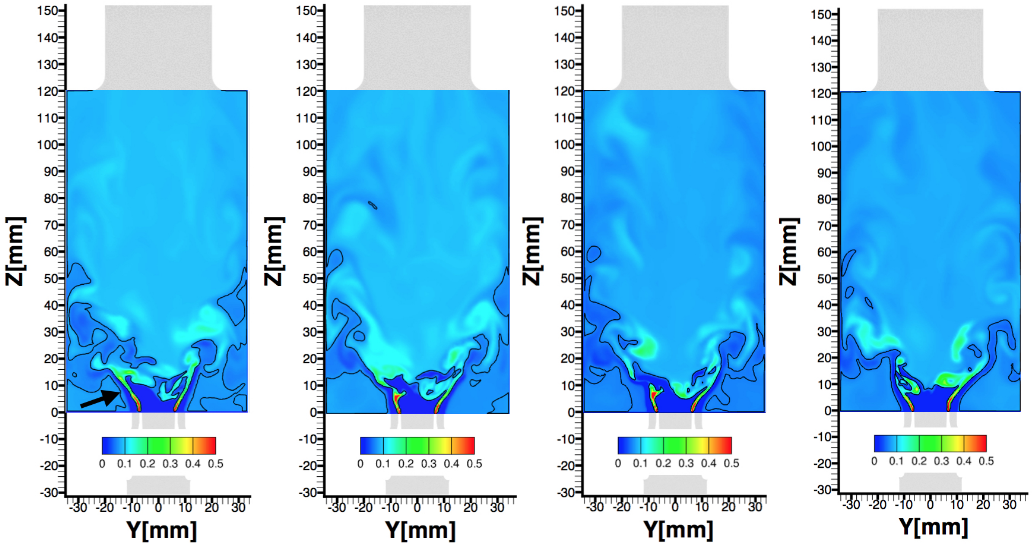

Figure 5: Snapshots of mixture fraction for 3 bar case (no sidejet), proceeding from left to right in 5 ms increments. Solid lines show stoichiometric mixture fraction (0.064). Arrow indicates the flapping jet arm.

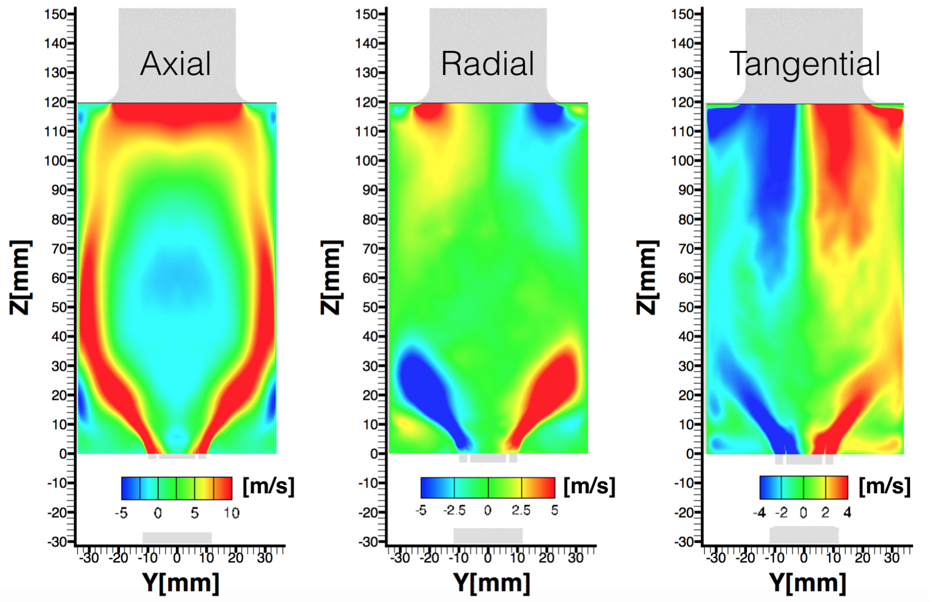

(a) 3 bar

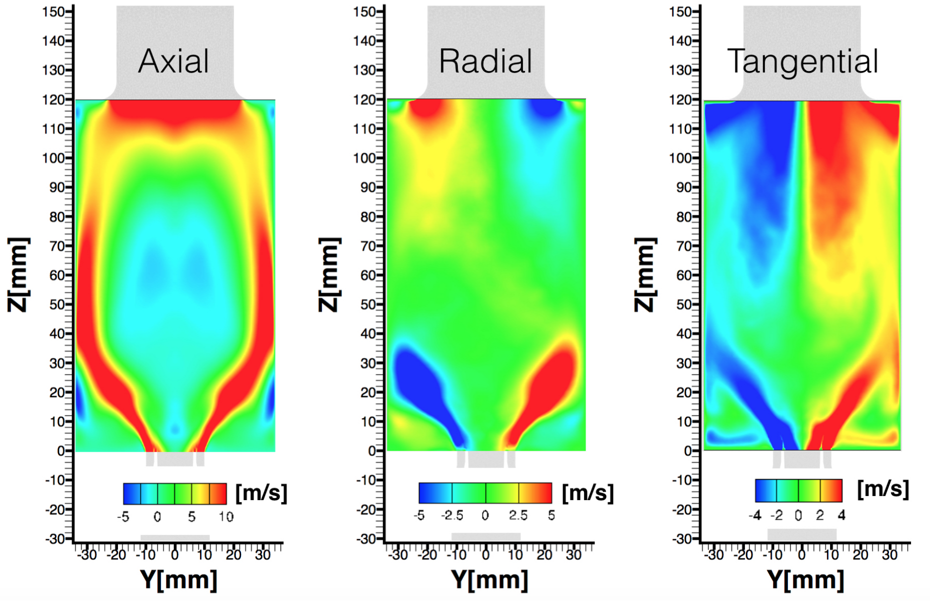

(b) 5 bar

Figure 6: Time-averaged velocity contour for 3 and 5 bar cases without sidejet.

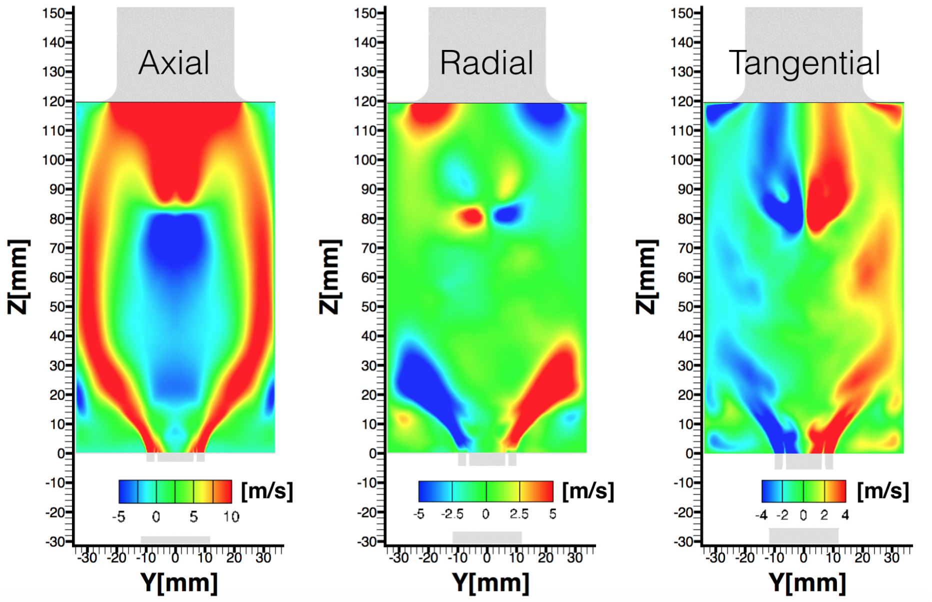

(a) 3 bar

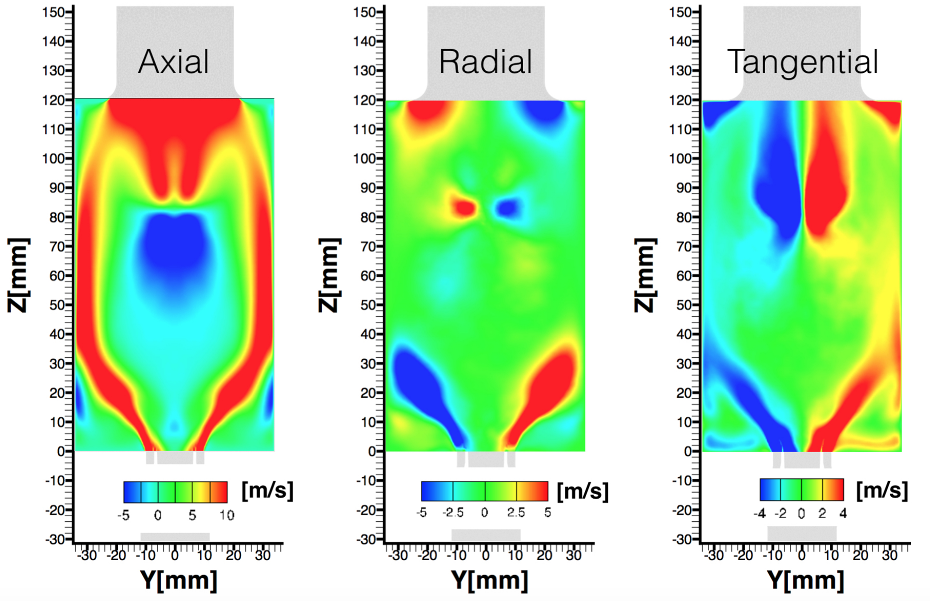

(b) 5 bar

Figure 7: Time-averaged velocity contour for 3 and 5 bar cases with sidejet.

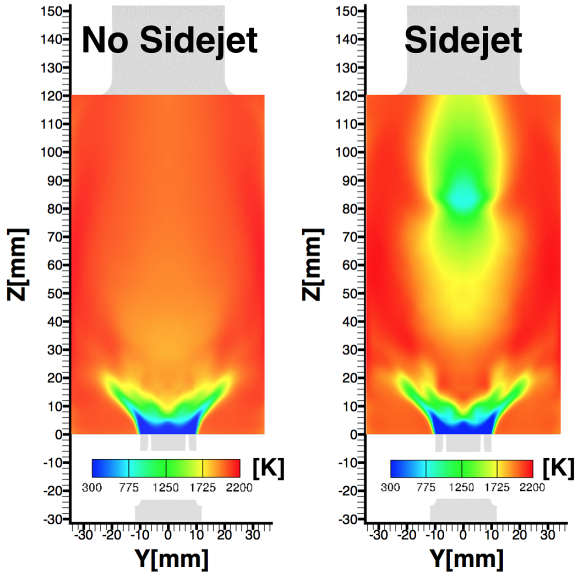

(a) 3 bar

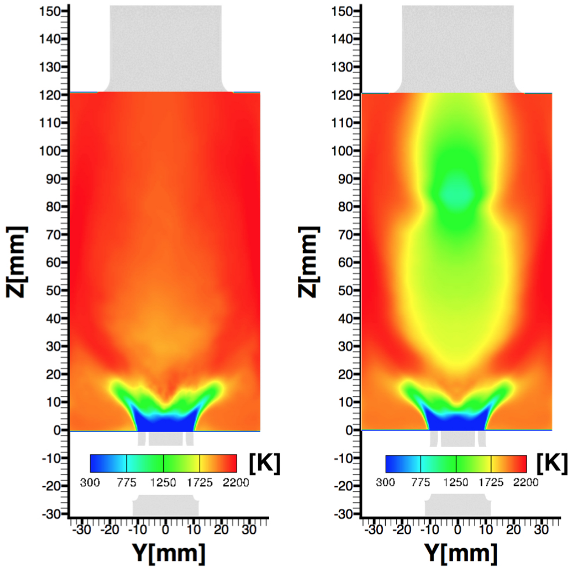

(b) 5 bar

Figure 8: Time-averaged temperature contour for 3 and 5 bar cases.

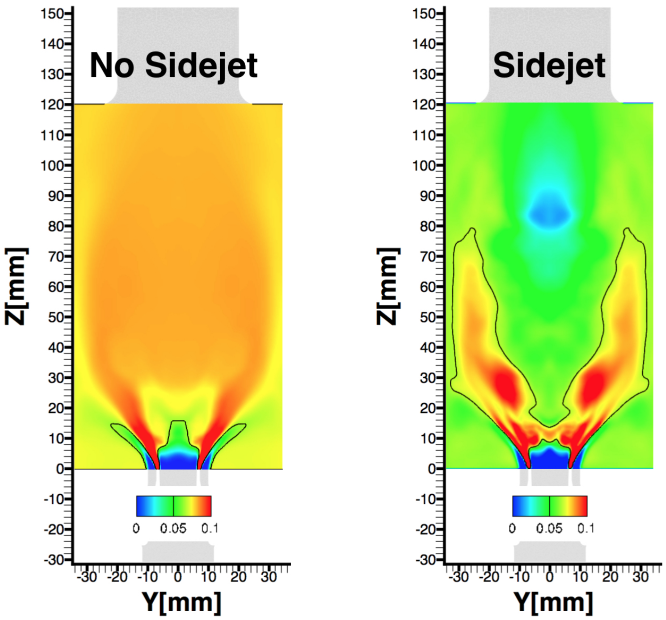

(a) 3 bar

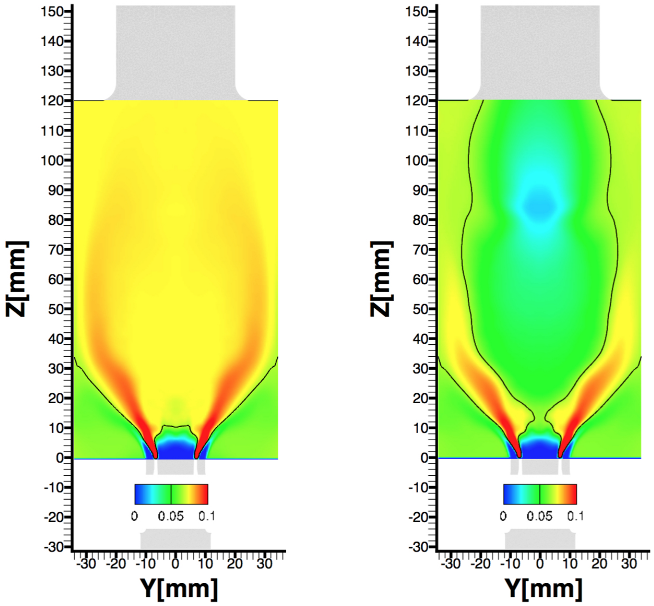

(b) 5 bar

Figure 9: Time-averaged mixture fraction contour for 3 and 5 bar cases. Solid lines show the stoichiometric mixture fraction (0.064).

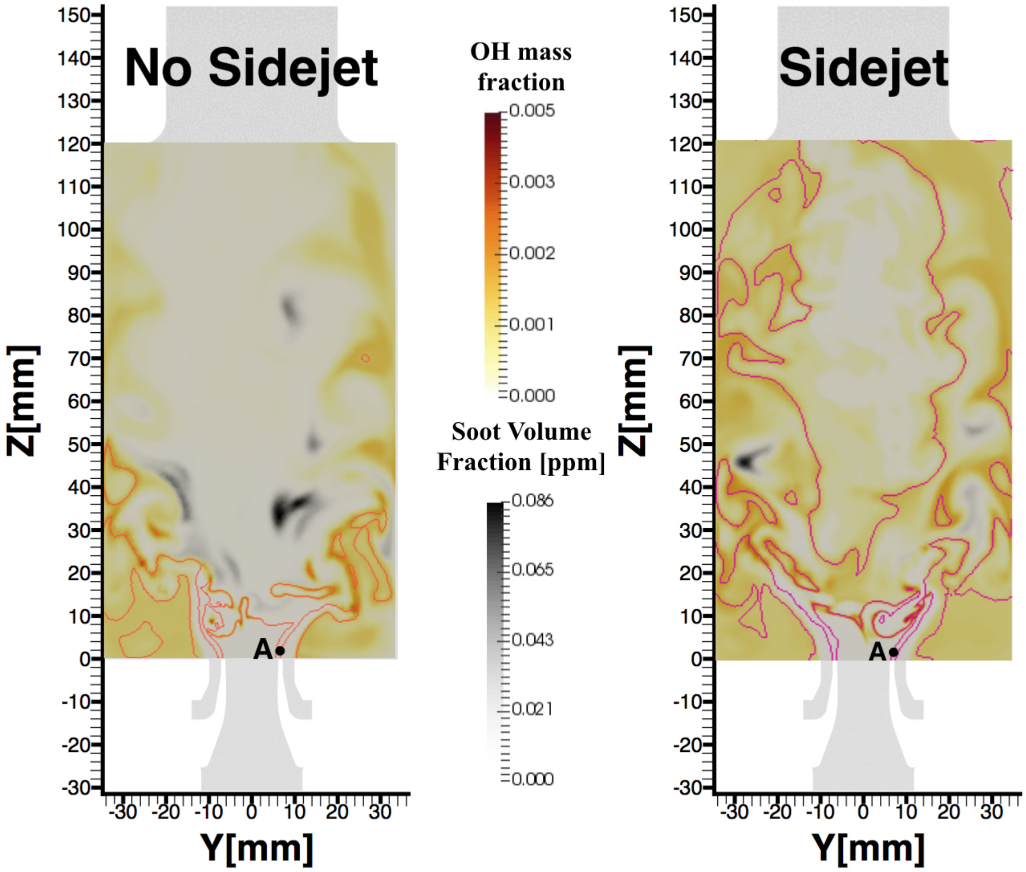

Figure 10: Instantaneous soot volume fraction overlaid with isocontour of OH mass fraction for 3 bar cases. Solid lines show the stoichiometric mixture fraction (0.064). Point A is the initial location from which particles are released for Lagrangian analysis.

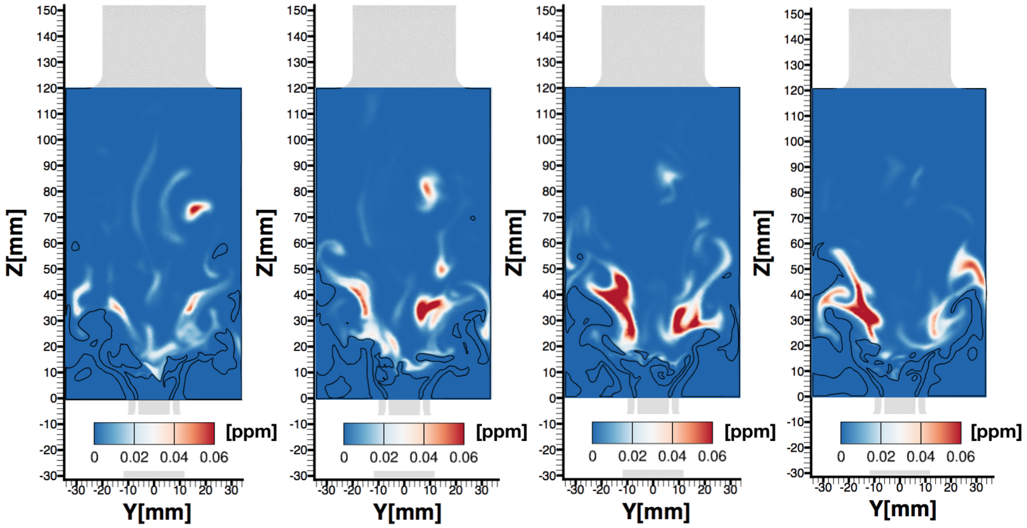

Figure 11: Instantaneous soot volume fraction snapshots of 3 bar case without sidejets, separated by 2.0 ms, and overlaid with stoichiometric mixture fraction (0.064) line.

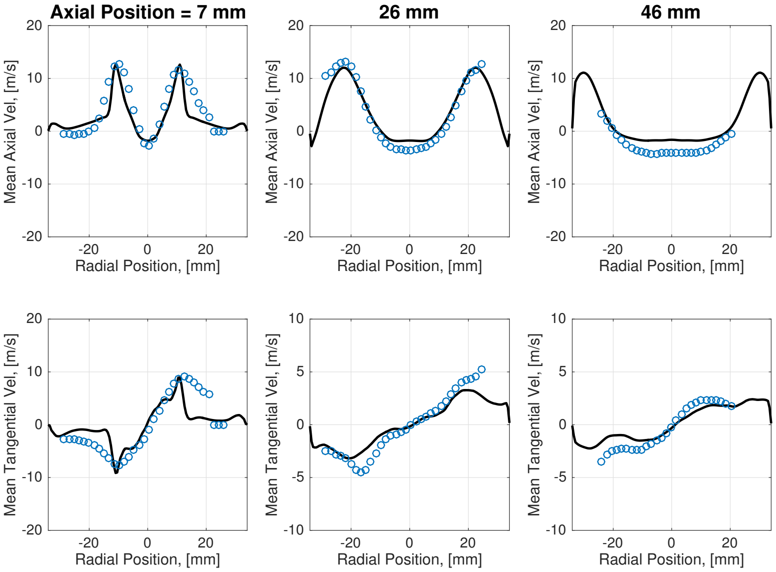

Figure 12: Time-averaged velocity comparison with experimental data for 3 bar case without sidejet.

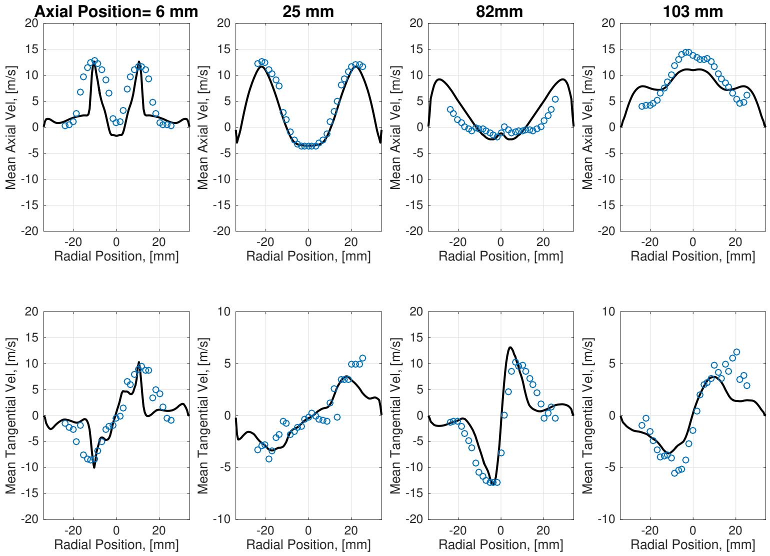

Figure 13: Time-averaged velocity comparison with experimental data for 3 bar case with sidejet.

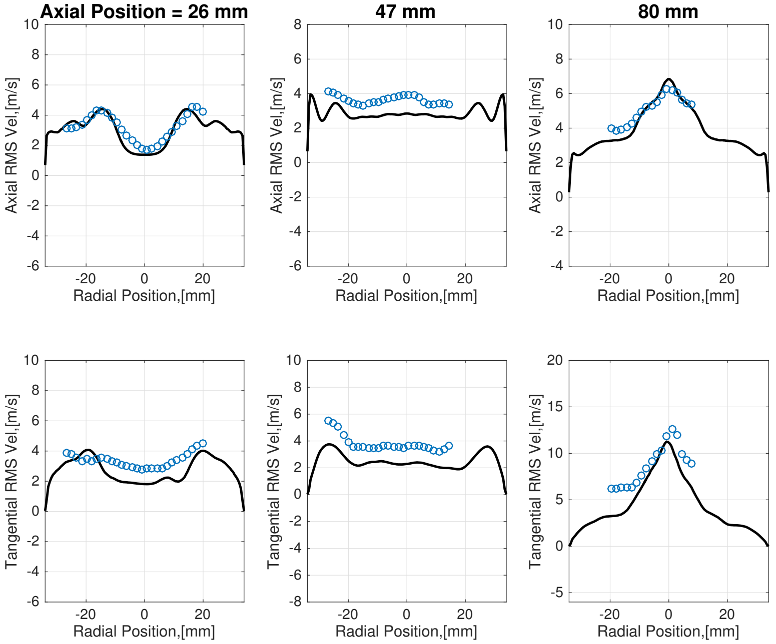

Figure 14: RMS velocity comparison with experimental data for 3 bar case with sidejet.

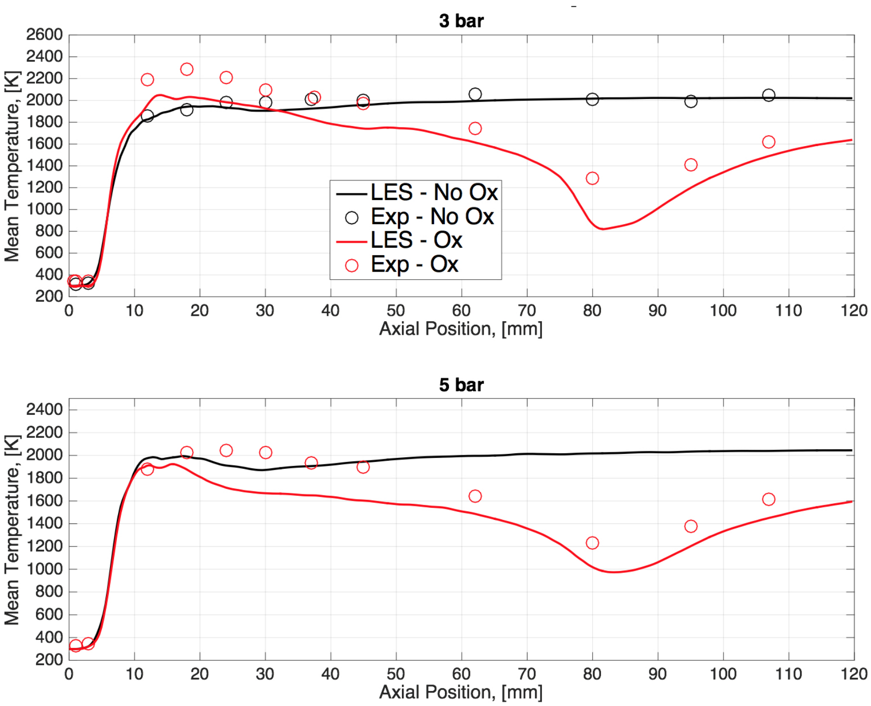

Figure 15: Mean centerline temperature comparisons of simulation with available experimental data for all cases. Note that no experimental data is available for the 5 bar case without sidejet.

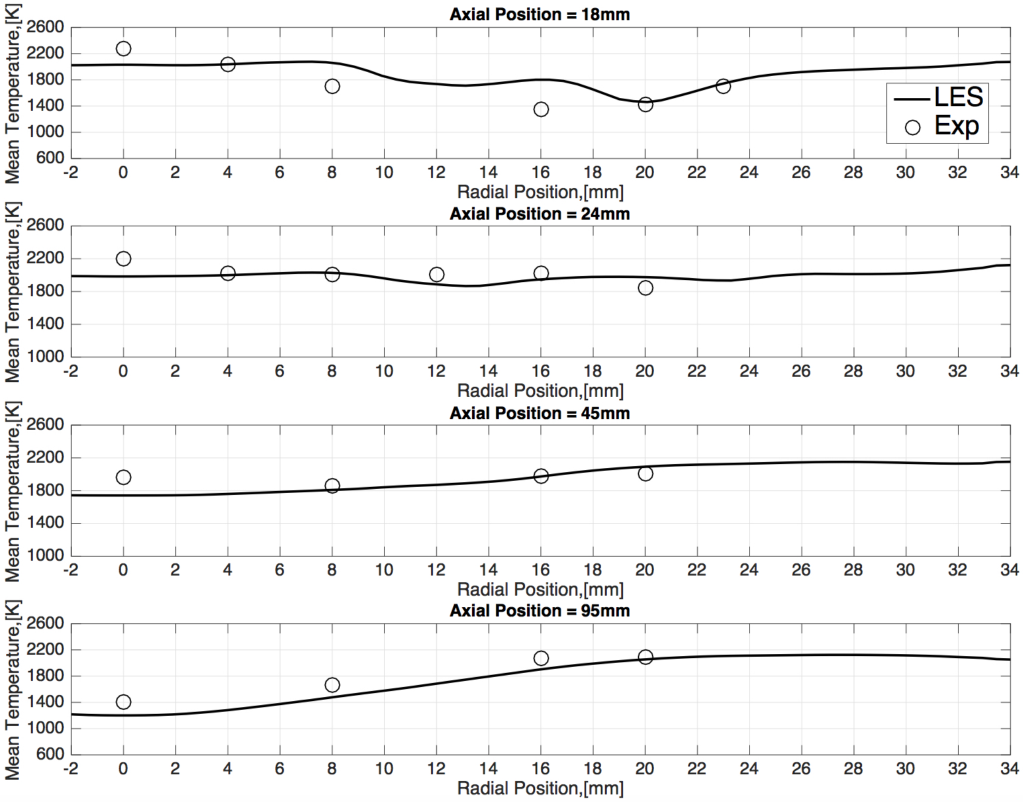

Figure 16: Mean radial temperature comparisons of simulation results with experimental data for 3 bar case with sidejet.

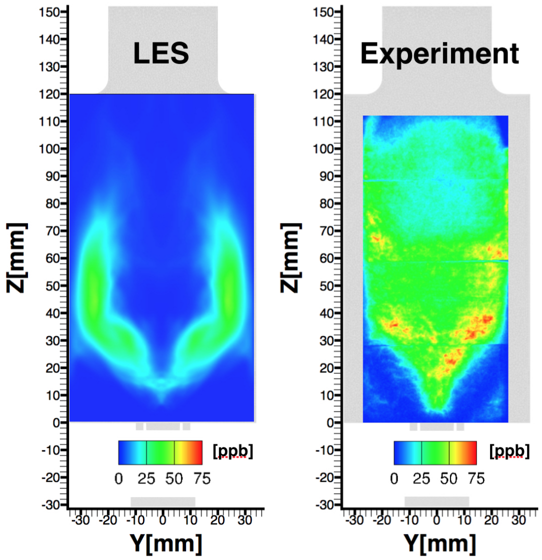

(a) No sidejet

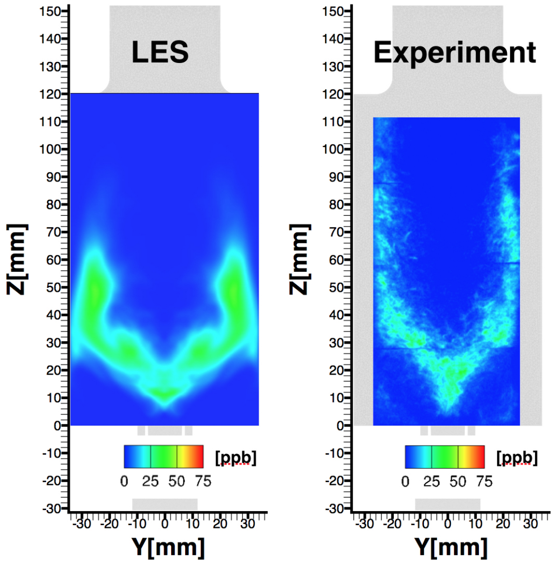

(b) Sidejet

Figure 17: Soot volume fraction comparison with experimental data for 3 bar case.

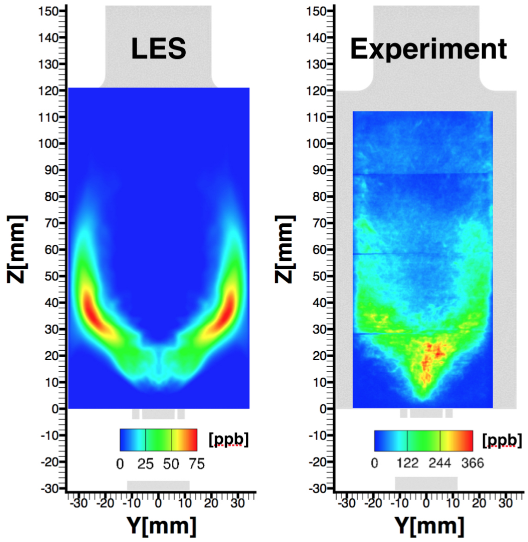

(a) No sidejet

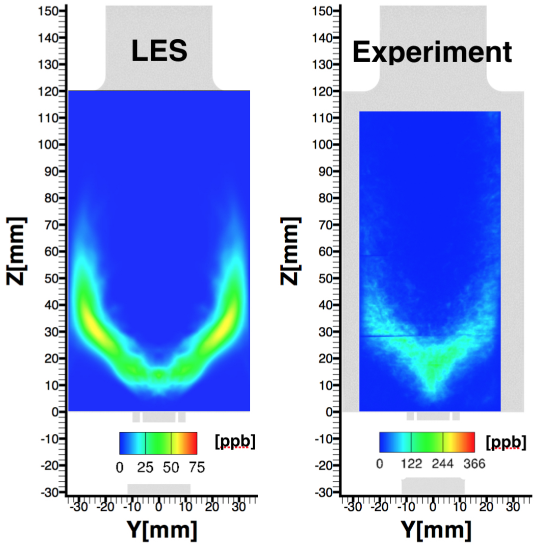

(b) Sidejet

Figure 18: Soot volume fraction comparison with experimental data for 5 bar case. Note the difference in contour color limits of approximately a factor of 5.0 between LES and experiment.

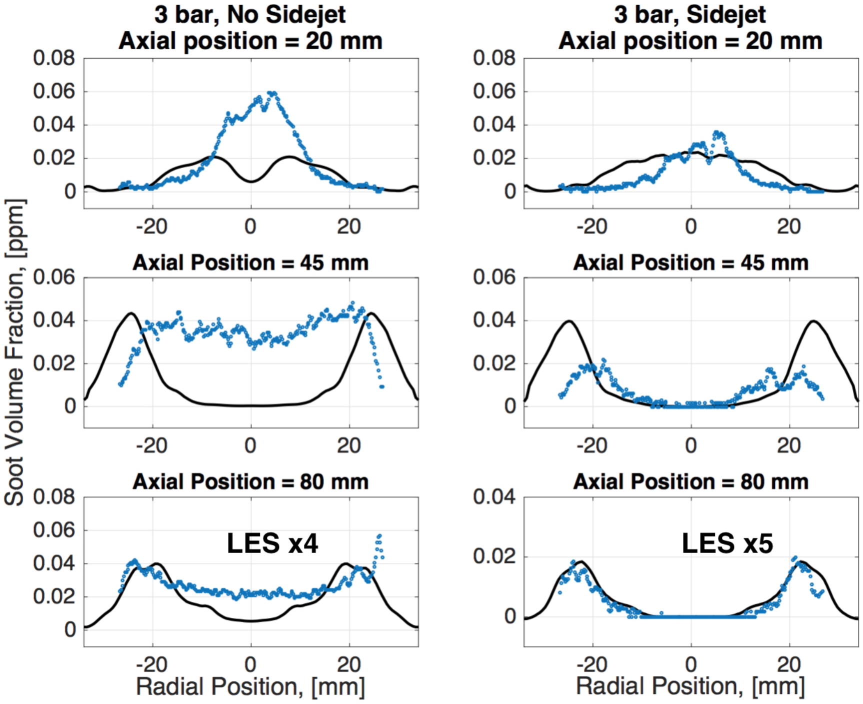

Figure 19: Soot volume fraction comparison of LES (line) with experimental data (scatter) for 3 bar case. LES results are multiplied by the corresponding factors as indicated in the figures only for the 80 mm axial position.

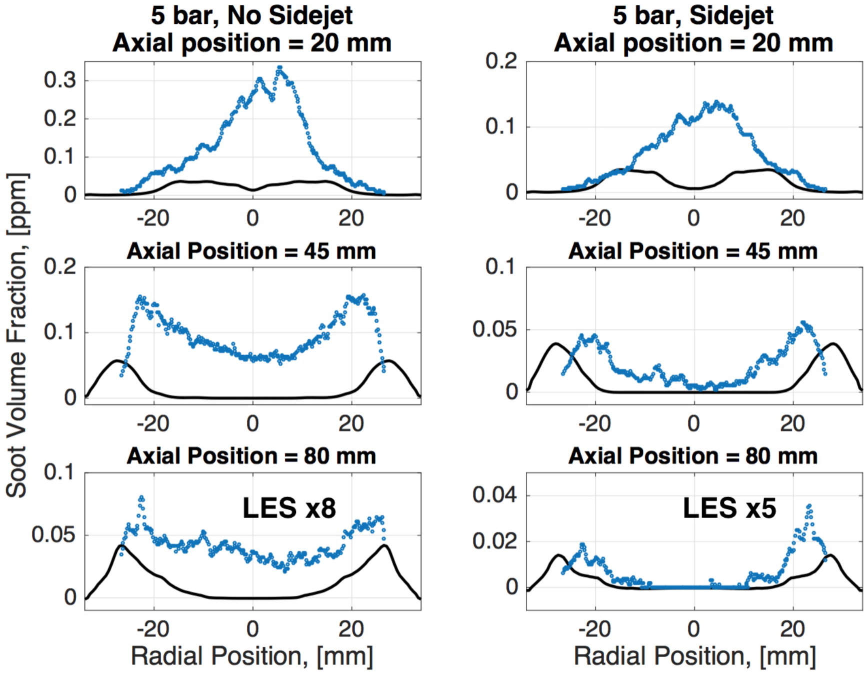

Figure 20: Soot volume fraction comparison of LES (line) with experimental data (scatter) for 5 bar case. LES results are multiplied by the corresponding factors as indicated in the figures only for the 80 mm axial position.

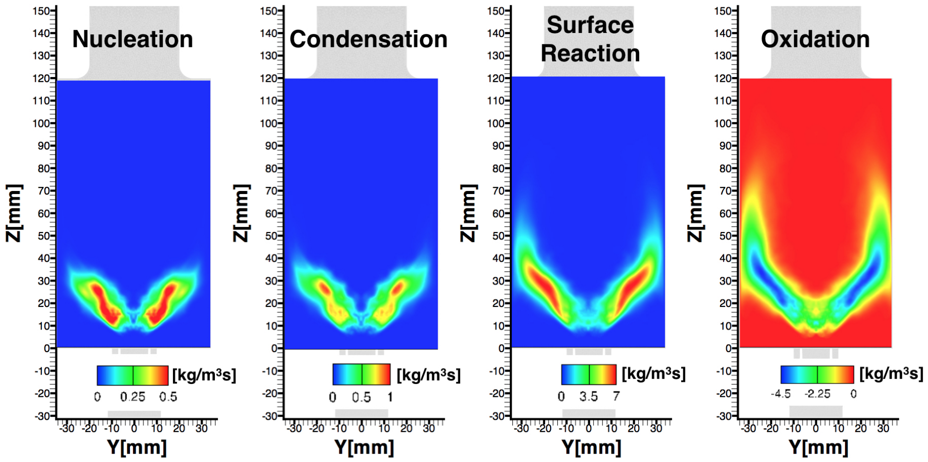

(a) No Sidejet

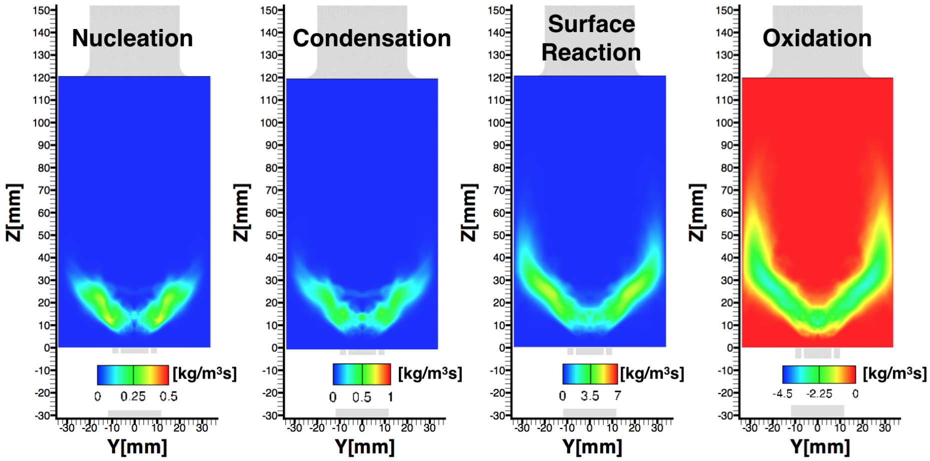

(b) Sidejet

Figure 21: Time-averaged soot volume fraction source terms comparison for 5 bar case.

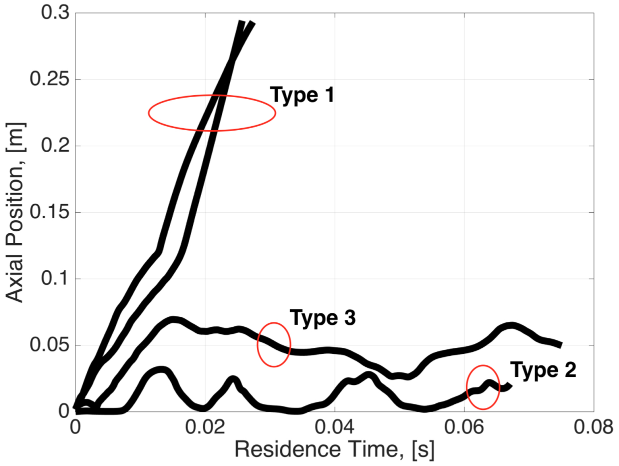

(a) Particle trajectory

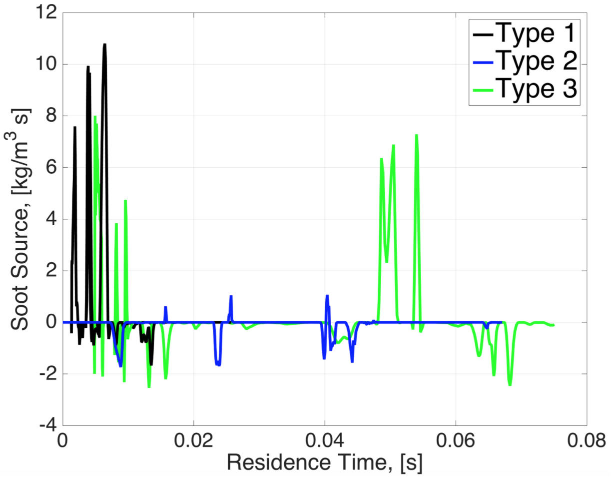

(b) Soot source

Figure 22: Lagrangian particle tracking of 4 example particles showing (a) particle trajectory by type, and (b) intermittent soot source, for 3 bar case without sidejet. Soot source includes nucleation, condensation, surface growth, and oxidation reactions.

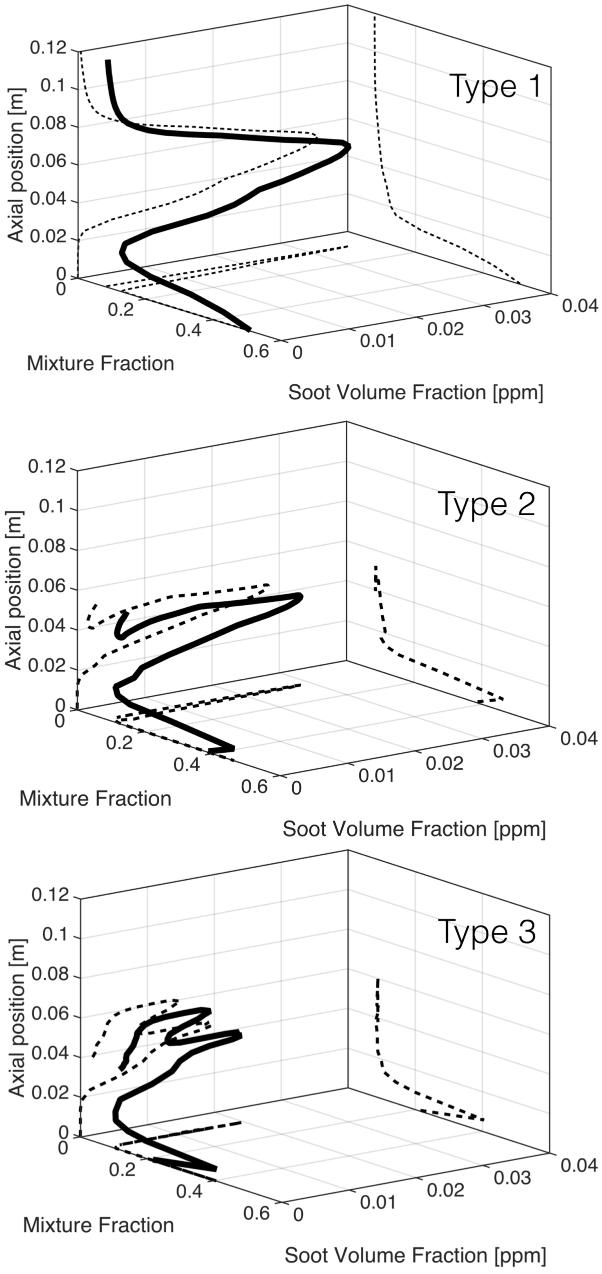

Figure 23: Ensemble averaged axial position, mixture fraction and soot volume fraction of lagrangian particles, by particle type, for 3 bar case without sidejet. Particle data was taken over the first 20 ms residence time for clearer visualization of the trajectory of the particle. Dashed line are projected trajectory onto the corresponding plane.

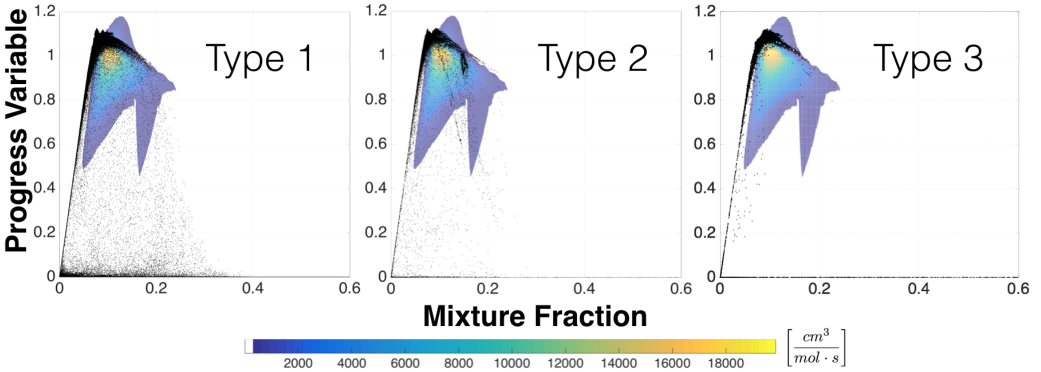

(a) 3 bar

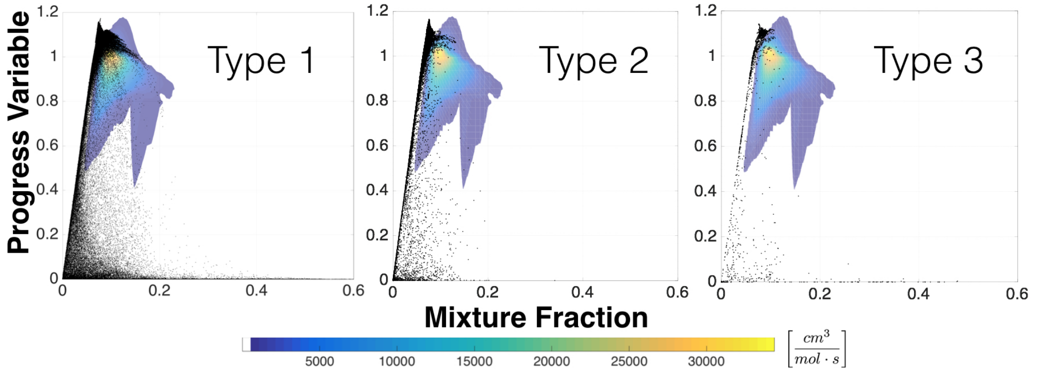

(b) 5 bar

Figure 24: Comparisons of lagrangian particle trajectories (scatter) in progress variable-mixture fraction phase space by particle type for 3 and 5 bar cases, without sidejet. Colored contour of soot surface growth rate is shown in the background with corresponding color legend.

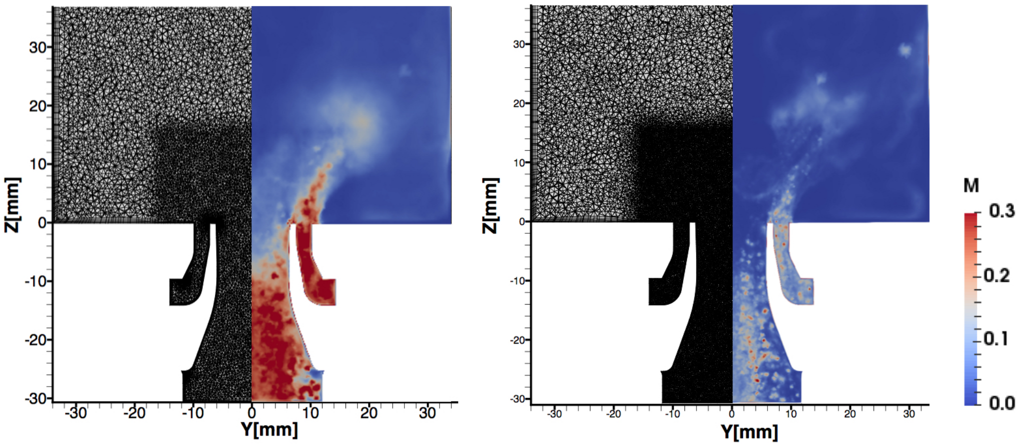

(a) 6 million mesh **(b) 12 million mesh**

Figure 25: Pope's criterion as a fraction of sub-filter kinetic energy over the total kinetic energy for the coarse and dense mesh with refinement at the centerline inlet core.

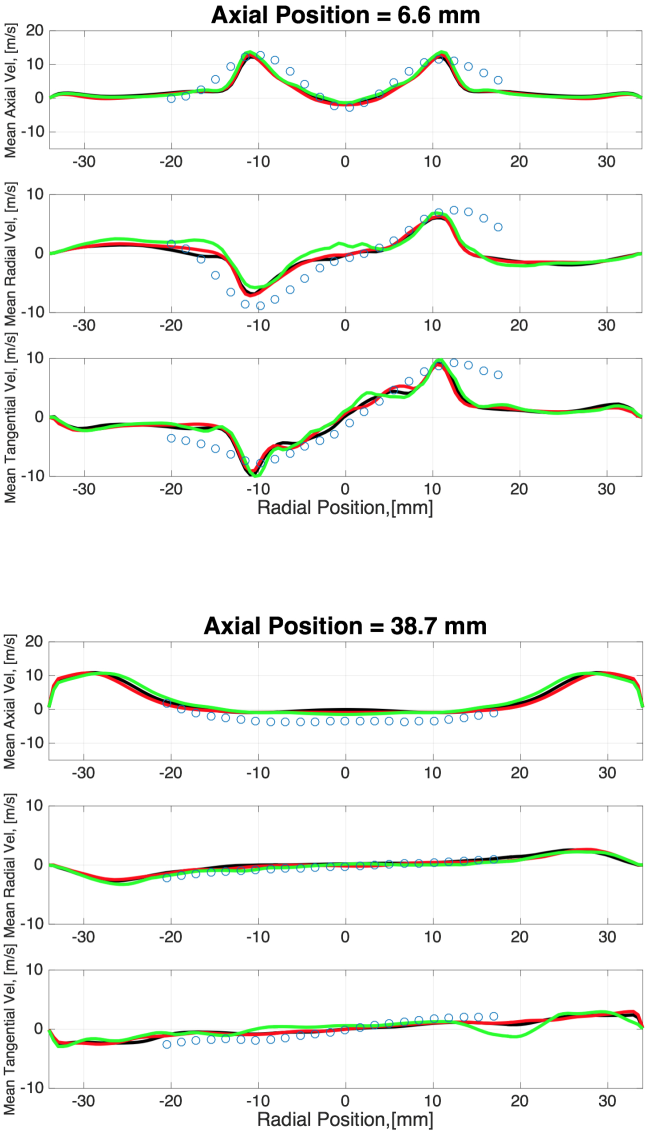

Figure 26: Velocity convergence test for the 3 bar case without sidejet at 6 million (black line), 12 million (red line), and 77 million (green line) mesh with experimental data (circle).

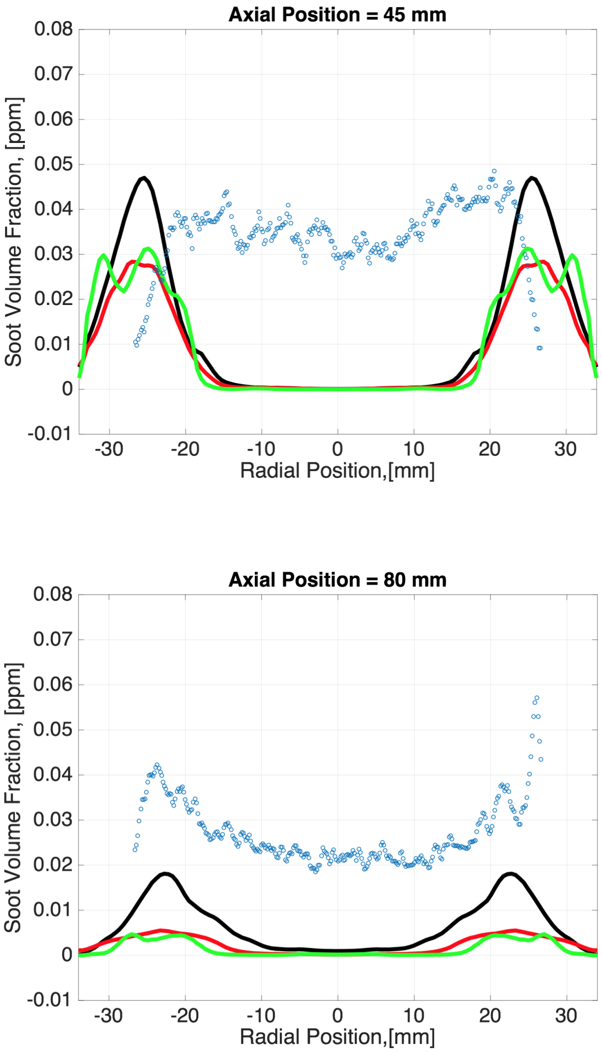

Figure 27: Soot volume fraction convergence test for the 3 bar case without sidejet at 6 million (black line), 12 million (red line), and 77 million (green line) mesh with experimental data (circle).

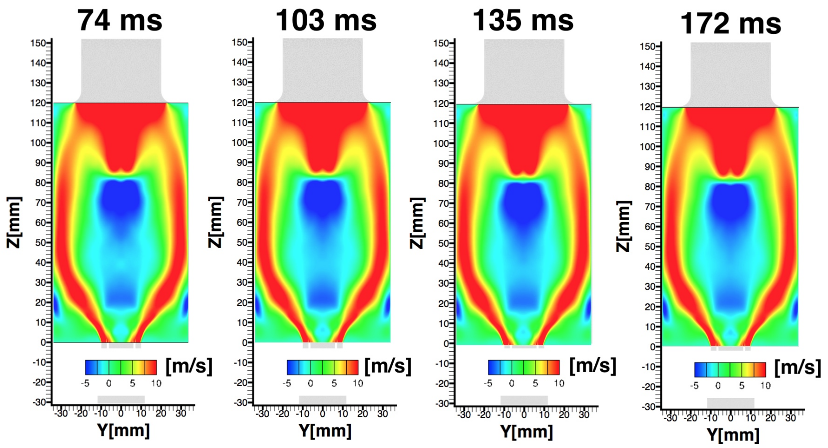

(a) Mean Axial Velocity

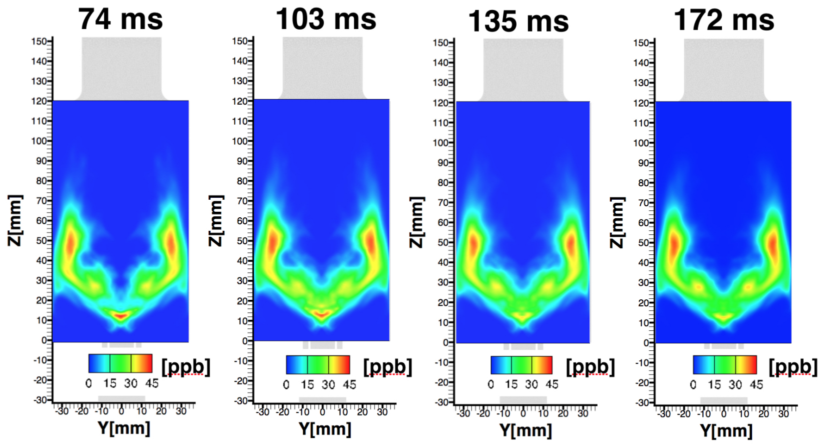

(b) Mean Soot Volume Fraction

Figure 28: Timeline of convergence for mean axial velocity and soot volume fraction for 3 bar pressure with sidejet.

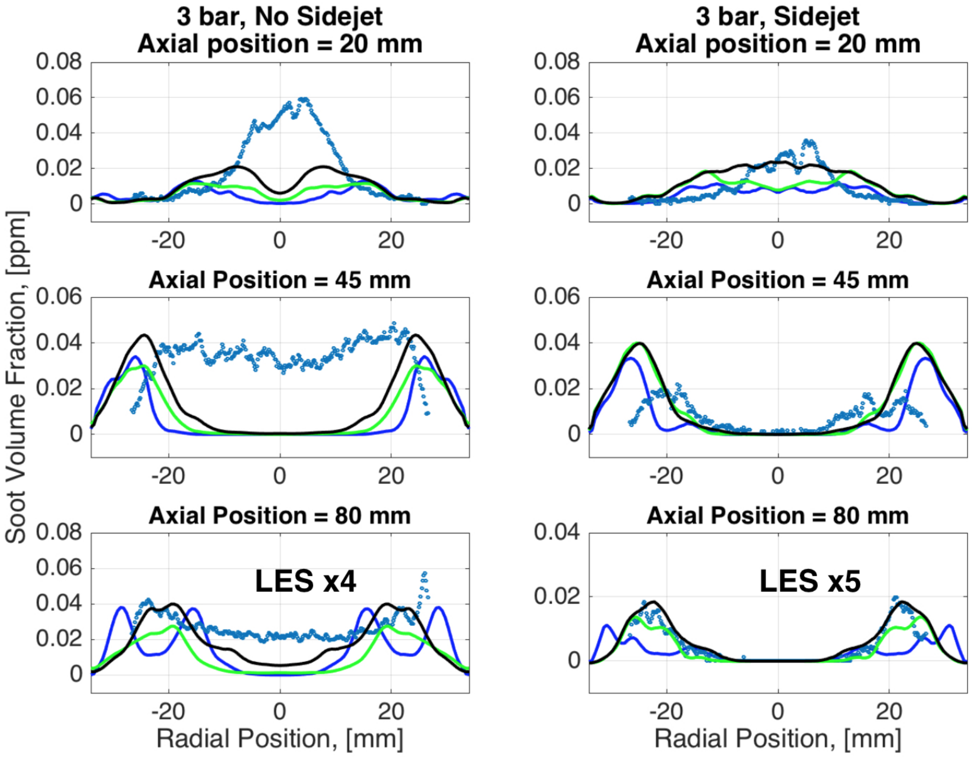

Figure 29: Mean soot volume fraction and convergence timeline for 3 bar case compared to experimental data (scatter). LES simulation lines with total averaging times of 70 ms (blue), 140 ms (green), and 200 ms (black) are shown.

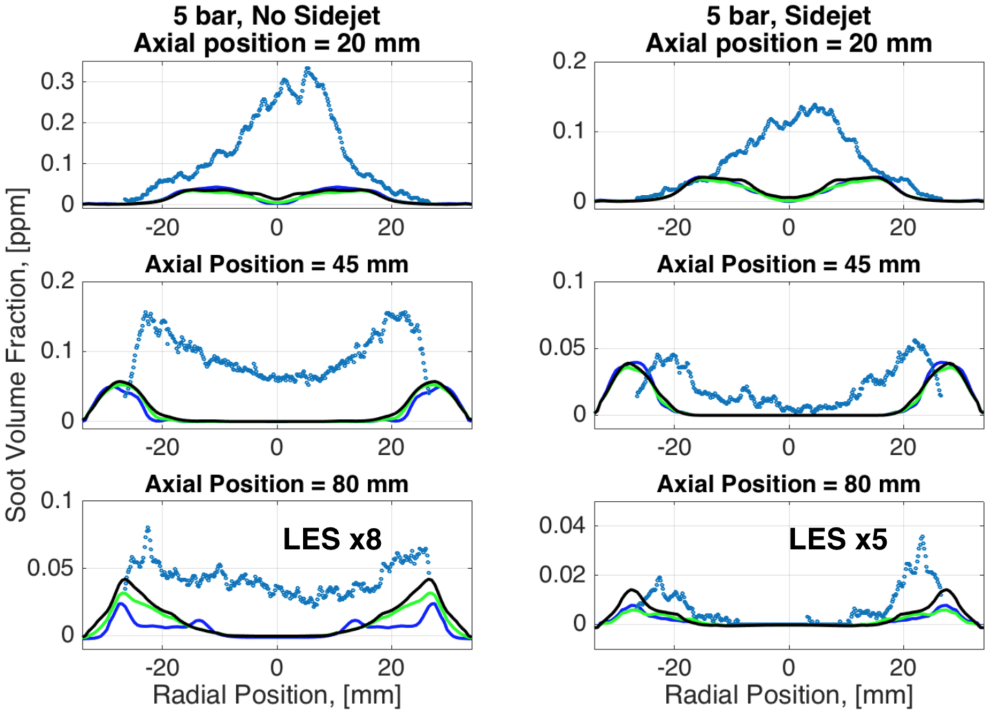

Figure 30: Mean soot volume fraction and convergence timeline sequence for 5 bar case compared to experimental data (scatter). LES simulation lines with total averaging times of 70 ms (blue), 140 ms (green), and 200 ms (black) are shown.